# The SEGUE Stellar Parameter Pipeline. I. Description and Initial Validation Tests

Young Sun Lee, Timothy C. Beers, Thirupathi Sivarani

*Department of Physics & Astronomy,*
*CSCE: Center for the Study of Cosmic Evolution,*
*and JINA: Joint Institute for Nuclear Astrophysics,*
*Michigan State University, East Lansing, MI 48824, USA*

`lee@pa.msu.edu, beers@pa.msu.edu, thirupathi@pa.msu.edu`

Carlos Allende Prieto, Lars Koesterke

*Department of Astronomy,*
*University of Texas, Austin, TX 78712*

`callende@astro.as.utexas.edu`

Ronald Wilhelm

*Department of Physics,*
*Texas Tech University, Lubbock, TX 79409*

`ron.wilhelm@ttu.edu`

John E. Norris

*Research School of Astronomy and Astrophysics,*
*The Australian National University, Weston, ACT 2611, Australia*

`jen@mso.anu.edu.au`

Coryn A. L. Bailer-Jones, Paola Re Fiorentin

*Max-Planck-Institute für Astronomy, Königstuhl 17, D-69117, Heidelberg, Germany*

`calj@mpia-hd.mpg.de, fiorent@mpia-hd.mpg.de`

Constance M. Rockosi

*Department of Astronomy,*
*University of California, Santa Cruz, CA 95064*

`crockosi@ucolick.org`

Brian Yanny

*Fermi National Accelerator Laboratory,*
*Batavia, IL 60510*

yanny@fnal.gov

Heidi J. Newberg

*Department of Physics & Astronomy,*
*Rensselaer Polytechnical Institute, Troy, NY 12180*

newbeh@rpi.edu

Kevin R. Covey

*Harvard-Smithsonian Center for Astrophysics,*
*60 Garden Street, Cambridge, MA 02138*

kcovey@cfa.harvard.edu

## ABSTRACT

We describe the development and implementation of the SEGUE (Sloan Extension for Galactic Exploration and Understanding) Stellar Parameter Pipeline (SSPP). The SSPP derives, using multiple techniques, radial velocities and the fundamental stellar atmospheric parameters (effective temperature, surface gravity, and metallicity) for AFGK-type stars, based on medium-resolution spectroscopy and *ugriz* photometry obtained during the course of the original Sloan Digital Sky Survey (SDSS-I) and its Galactic extension (SDSS-II/SEGUE). The SSPP also provides spectral classification for a much wider range of stars, including stars with temperatures outside of the window where atmospheric parameters can be estimated with the current approaches. This is Paper I in a series of papers on the SSPP; it provides an overview of the SSPP, and initial tests of its performance using multiple data sets. Random and systematic errors are critically examined for the current version of the SSPP, which has been used for the sixth public data release of the SDSS (DR-6).

*Subject headings:* methods: data analysis — stars: abundances, fundamental parameters — surveys — techniques: spectroscopic

## 1. Introduction

The Sloan Extension for Galactic Understanding and Exploration (SEGUE) is one of three surveys that are being executed as part of the current extension of the Sloan Digital Sky Survey (SDSS-II), which consists of LEGACY, SUPERNOVA SURVEY, and SEGUE. The SEGUE program is designed to obtain *ugriz* imaging of some 3500 square degrees of sky outside of the original SDSS-I footprint (Fukugita et al. 1996; Gunn et al. 1998, 2006; York et al. 2000; Stoughton et al. 2002; Abazajian et al. 2003, 2004, 2005; Pier et al. 2003; Adelman-McCarthy et al. 2006, 2007a). The regions of sky targeted are primarily at lower Galactic latitudes ($|b| < 35°$), in order to better sample the disk/halo interface of the Milky Way. As of Data Release 6 (DR-6, Adelman-McCarthy et al. 2007b), about 85% of the planned additional imaging has already been completed. SEGUE is also obtaining $R \simeq 2000$ spectroscopy, over the wavelength range $3800 - 9200$ Å, for some 250,000 stars in 200 selected areas over the sky available from Apache Point, New Mexico. The spectroscopic candidates are selected on the basis of *ugriz* photometry to populate roughly 16 target categories, chosen to explore the nature of the Galactic stellar populations at distances from 0.5 kpc to over 100 kpc from the Sun. Spectroscopic observations have been obtained for roughly half of the planned targets thus far, a total of about 120,000 spectra. The SEGUE data clearly require automated analysis tools in order to efficiently extract the maximum amount of useful astrophysical information for the targeted stars, in particular their stellar atmospheric parameters, over wide ranges of effective temperature ($T_{\rm eff}$), surface gravity (log $g$), and metallicity ([Fe/H]).

Numerous methods have been developed in the past in order to extract atmospheric-parameter estimates from medium-resolution stellar spectra in a fast, efficient, and automated fashion. These approaches include techniques for finding the minimum distance (parameterized in various ways) between observed spectra and grids of synthetic spectra (e.g., Allende Prieto et al. 2006), non-linear regression models (e.g., Re Fiorentin et al. 2007, and references therein), correlations between broadband colors and the strength of prominent metallic lines, such as the Ca II K line (Beers et al. 1999), auto-correlation analysis of a stellar spectrum (Beers et al. 1999, and references therein), obtaining fits of spectral lines (or summed line indices) as a function of broadband colors (Wilhelm et al. 1999), or the behavior of the Ca II triplet lines as a function of broadband color (Cenarro et al. 2001a,b). However, each of these approaches exhibits optimal behavior only over restricted temperature and metallicity ranges; outside of these regions they are often un-calibrated, suffer from saturation of the metallic lines used in their estimates at high metallicity or low temperatures, or lose efficacy due to the weakening of metallic species at low metallicity or high temperatures. The methods that make use of specific spectral features are susceptible to other problems, e.g., the presence of emission in the core of the Ca II K line for chromo-

spherically active stars, or poor telluric line subtraction in the region of the Ca II triplet. Because SDSS stellar spectra cover most of the entire optical wavelength range, one can apply several approaches, using different wavelength regions, in order to glean optimal information on stellar parameters. The combination of multiple techniques results in estimates of stellar parameters that are more robust over a much wider range of $T_{\mathrm{eff}}$, log $g$, and [Fe/H] than those that might be produced by individual methods. In this first paper of a series, we describe the SEGUE Stellar Parameter Pipeline (hereafter, SSPP), which implements this "multi-method" philosophy. We also carry out a number of tests to assess the range of stellar atmospheric parameter space over which the estimates obtained by the SSPP remain valid. The second paper in the SSPP series (Lee et al. 2007b; hereafter Paper II) seeks to validate the radial velocities and stellar parameters determined by the SSPP by comparison with member stars of Galactic three globular clusters (M 15, M 13, and M 2) and two open clusters (NGC 2420 and M 67). A comparison with an analysis of high-resolution spectra for SDSS-I/SEGUE stars is presented in the third paper in this series (Allende Prieto et al. 2007; hereafter Paper III).

Section 2 describes determinations of radial velocity used by the SSPP. The procedures used to obtain an estimate of the appropriate continuum, and the determination of line indices, is explained in §3. The methods that the SSPP employs for determining stellar parameters are presented in §4. Section 5 addresses the determinations of auxiliary estimates of effective temperature, based on both theoretical and empirical approaches; these methods are used for stars where adequate estimates of $T_{\mathrm{eff}}$ are not measured by our primary techniques. A decision tree that gathers the optimal set of parameter estimates based on the multiple methods is introduced in §6. Section 7 summarizes the conditions for raising various flags to warn potential users where uncertainties in parameter determinations remain. In §8, we discuss validation of the parameters determined by the SSPP based on SDSS-I/SEGUE stars for which we have obtained higher dispersion spectroscopy on various large telescopes, and also compare the parameters with those of likely member stars of Galactic open and globular clusters. Assignments of approximate MK spectral classifications are described in §9. In §10 we describe several methods (still under testing) for the determination of distance estimates used by the SSPP. Section 11 presents a summary and conclusions.

In the following, the colors ($u - g$, $g - r$, $r - i$, $i - z$, and $B - V$) and magnitudes ($u$, $g$, $r$, $i$, $z$, $B$, and V) are understood to be de-reddened and corrected for absorption (using the dust maps of Schlegel et al. 1998), unless stated specifically otherwise.

## 2. Determinations of Radial Velocities

## 2.1. The Adopted Radial Velocities Used by the SSPP

The *spZbest* fits file, which is generated from the SDSS spectroscopic reduction pipeline, provides two estimated radial velocities. One is an absorption-line redshift computed from a cross-correlation procedure using templates that were obtained from SDSS commissioning spectra (Stoughton et al. 2002). Another estimate comes from performing a "best-match" procedure that compares the observed spectra with externally measured templates (in this case, the ELODIE library high-resolution spectra, as described by Prugniel & Soubiran 2001), degraded to match the resolving power of SDSS spectra.

Previous experience with the analysis of SDSS stellar spectra suggested that the radial velocity estimated from the ELODIE template matches is often the best available estimate, in the sense that it is the most repeatable, based on spectra of "quality assurance" stars with multiple determinations. However, there are some cases where the quoted error of an ELODIE spectral match velocity is larger than expected; hence we also make use of the cross-correlation radial velocity, in the following manner. If the velocity determined by comparison with the ELODIE templates has a reported error of 20 km s$^{-1}$ or less, then this velocity is adopted and the radial velocity flag is set to 'RVOK(20)'. If the error from the ELODIE template comparison is larger than 20 km s$^{-1}$ and the relative difference between the two reported radial velocities is less than 40 km s$^{-1}$, then we take an average of the two techniques, and the radial velocity flag is set to 'RVOK(40)'. If the error in the reported ELODIE velocity is larger than 20 km s$^{-1}$, and the difference of between the two estimates is between 40 and 100 km s$^{-1}$, we take an average of the two and the radial velocity flag is set to 'RVOK(100)'.

If none of the above conditions are satisfied (which happens only rarely, and mainly for quite low $S/N$ spectra, or for hot/cool stars without adequate templates), then we obtain an independent estimate of the radial velocity based on our own IDL routines. The calculation of the radial velocity is carried out by determining wavelength shifts for several strong absorption line features (Ca II K, Ca II H, H$\delta$, Ca I, H$\gamma$, H$\beta$, Na I, H$\alpha$, and Ca II triplet). After ignoring the calculated velocity above +500 km s$^{-1}$ or below −500 km s$^{-1}$ from the individual lines (which are very often spurious), we obtain a $3\sigma$-clipped average of the remaining radial velocities. If this computed average falls between −500 km s$^{-1}$ and +500 km s$^{-1}$, we take the calculated radial velocity as the adopted radial velocity and set the radial velocity flag to 'RVCALOK'. We have noticed that certain types of stars, in particular cool stars with large carbon enhancements, present a challenge for the radial velocity estimates obtained by the SSPP. We have developed new carbon-enhanced templates, based on syn-

thetic spectra, which appear to return improved estimates. These will be implemented in the next major update of the SSPP, which we anticipate applying for the next data release, DR-7.

It should be noted that many of the techniques used for atmospheric parameter estimation in the SSPP work well even when the velocity determination for a given star has errors of up to 100 km s$^{-1}$ or more. The reason for this is that many of our methods compare a wide spectral range with the synthetic spectra, rather than a line-by-line comparison, to determine stellar parameters. Even for those techniques that employ line-index approaches, the SSPP employs relatively wide bandwidths, which will tend to mitigate small variations due to radial velocity errors. Thus, small shifts in a spectrum due to a poor radial velocity determination will not strongly influence our estimates of the stellar parameters. Hence, we choose not to ignore spectra with high velocity errors, but rather, indicate caution with the appropriate radial velocity flag.

If none of the above methods yields an acceptable estimate of radial velocity, or if the reported velocity is apparently spurious (greater than 1000 km s$^{-1}$ or less than $-1000$ km s$^{-1}$), we simply ignore the spectrum of the star in our subsequent analysis, and set the radial velocity flag to 'RVNOTOK'.

## 2.2.   Checks on Radial Velocities – Zero Points and Scatter

In order to check on the accuracy of the radial velocities adopted by the SSPP, we compare with over 150 high-resolution spectra of SDSS-I/SEGUE stars that have been obtained in order to calibrate and validate the stellar atmospheric parameters. Table 1 summarizes the available high-resolution data. We plan to continue enlarging this sample of validation/calibration stars in the near future.

The high-resolution spectra have been reduced and analyzed independently by two of the present authors (C. A. and T.S.). A detailed discussion is presented in Paper III. During the course of deriving the stellar parameter estimates from the high-resolution spectra, the radial velocities of stars are first measured. Note that C.A. only considered the HET spectra, while S.T. considered all available spectra. Thus, only the HET stars have radial velocities obtained by both analysts; for these stars we take an average of their independent determinations, which typically differ by no more than $1-2$ km s$^{-1}$. A more detailed discussion is presented in Paper III.

After rejecting problematic spectra (e.g., low $S/N$ high-resolution spectra, or stars that appear to be spectroscopic binaries at high spectral resolution), 125 stars remain to compare

with the adopted radial velocity results from the SSPP. Figure 1 shows the results of these comparisons. A consistent offset of $-6.94$ km s$^{-1}$ (with a standard deviation of 4.82 km s$^{-1}$) is computed from a Gaussian fit to the residuals; this offset appears constant over the color range $0.1 \leq g - r \leq 0.9$. An additional comparison with the radial-velocity distribution of likely member stars in the Galactic globular clusters M 15 and M 13 reveals similar offsets ($-6.8$ km s$^{-1}$ and $-8.6$ km s$^{-1}$, respectively; see Paper II). The origin of this velocity offset might stem from different algorithms in the line fits to arc and sky lines (Adelman-McCarthy et al. 2007b). It should be noted that an offset of $+7.3$ km s$^{-1}$ is added to all DR-6 (Adelman-McCarthy et al. 2007b) stellar radial velocities. This offset was computed by averaging the offsets of $-6.8$ km s$^{-1}$(M 15) and $-8.6$ km s$^{-1}$(M 13), and the $-6.6$ km s$^{-1}$ offset that was obtained from a preliminary result of a high-resolution spectroscopic analysis of SDSS-I/SEGUE stars that was carried out prior to DR-6 (Adelman-McCarthy et al. 2007b). Now that a recent high-resolution spectroscopic analysis of SDSS-I/SEGUE stars (Paper III) indicates an offset of about $-6.9$ km s$^{-1}$, the average offset is $+7.4$ km s$^{-1}$. Therefore, in future data releases (e.g, DR-7), this very minor difference will likely be reflected in all adopted stellar radial velocities. However, in order to account for its presence and to be consistent with the DR-6 database, we apply this empirical $+7.3$ km s$^{-1}$ shift to each adopted radial velocity obtained by the SSPP. After application of this velocity shift, the zero-point uncertainties in the corrected radial velocities determined by the SSPP (and the SDSS spectroscopic reduction pipeline it depends on) should be close to zero, with a random scatter on the order of 5 km s$^{-1}$ or less. Note that the scatter in the determination of radial velocities, based on the average displacements of the "quality assurance" stars with multiple measurements varies from 5.0 km s$^{-1}$ to 9.0 km s$^{-1}$, depending on spectral type, and exhibits a scatter of 2 km s$^{-1}$ between observations obtained with the "faint" and "bright" spectroscopic plug-plates (Adelman-McCarthy et al. 2007b).

## 3. Calculation of Line Indices

The initial step in calculation of line indices for SDSS spectra is to transform the wavelength scale of the original SDSS spectrum over to an air-based (rather than vacuum-based) wavelength scale, and to linearly rebin the spectrum to 1 Å bins in the blue ($3800-6000$ Å), and 1.5 Å bins in the red ($6000-9000$ Å). This slightly larger bin size is due to the degradation of the resolution in the red regions of the spectra. Then, based on the adopted radial velocity described above, the wavelength scale is shifted to zero rest wavelength.

The SSPP measures line indices of 77 atomic and molecular lines. Line index calculations are performed in two modes; one uses a global continuum fit over the entire wavelength range

(3850−9000 Å), while the other obtains local continuum estimates around the line bands of interest. The choice between which mode is used depends on the line depth and width of the feature under consideration. Local continua are employed for the determinations of stellar atmospheric parameters based on techniques that depend on individual line indices. Other techniques, such as the neural network, spectral matching, and auto-correlation methods, require wider wavelength ranges to be considered; for these the global continuum is used. We make use of the errors in the fluxes reported by the SDSS spectroscopic reduction pipeline to measure the uncertainty in the line indices. Details of the procedures used to obtain the continuum fits and line index measures (and their errors) are discussed below.

## 3.1. Continuum Fit Techniques

### 3.1.1. Global Continuum Fit

Determination of the appropriate continuum for a given spectrum is a delicate task, even more so when it must be automated, and obtained for stars having wide ranges of effective temperatures, as is the case for the present application.

In order to obtain a global continuum fit, the SSPP first proceeds by fitting the stellar spectrum to a seventh-order polynomial. For wavelengths less than 6500 Å, if the observed flux is below that of the initial continuum fit in each pixel, we add the difference between the observed flux and initial continuum fit to the value of the continuum fit at each pixel. For wavelengths larger than 6500 Å, we overwrite the observed flux with the fitted continuum function (plus errors). This modified flux vector becomes the input for the next continuum estimate, again obtained by fitting a seventh order polynomial. This loop is iterated twice. The resultant continuum is considered the first-pass estimate of the global continuum level.

The reason for setting the wavelength cut to 6500 Å in the above algorithm is to guard against the effects of, e.g., low signal-to-noise data in the red for warmer stars, the peculiar flux distribution of extremely cool stars, or poor sky-line subtraction around the Ca II triplet in the SDSS pipeline (in some cases). We find that if we use the filtered flux for the first-pass continuum estimate, as above, we are better able to derive reasonable results in the red portion of the spectrum.

After obtaining the first-pass estimated continuum, we reject points in the modified flux vector that are more than $3\sigma$ above the fitted continuum, where $\sigma$ is the estimated error in the fitting function. The reason that we reject the points which are $3\,\sigma$ above the fitted line is to remove sky lines in the Ca II triplet region, which may remain in the modified flux vector even after obtaining the first-pass continuum estimate. Whether or not we reject

points that are $3\sigma$ below the first-pass continuum, there is not much difference in the final continuum determination. This is because, in the course of deriving the first-pass continuum, most of strong absorption lines are taken care of already. Following this step, a sixth-order polynomial fit to the $3\sigma$ clipped flux vector is carried out in order to obtain a second-pass continuum estimate. The final global continuum level is determined from a weighted sum of the two estimated continua (40% of the first-pass continuum level estimate is added to 60% of the second-pass continuum level estimate). The upper panel of Figure 2 shows an example of a fitted global continuum obtained in this manner. The bottom panel is the normalized spectrum, obtained by division of the spectrum by the global continuum fit. It can be seen that a reasonable continuum estimate is obtained even in the region of the Ca II triplet, where residuals from poor sky subtraction can sometimes be problematic.

### 3.1.2. Local Continuum Fit

To compute a local continuum over the line band of interest, we first calculate a $5\sigma$-clipped average of the fluxes over the (blue and red) sidebands corresponding to each feature, as listed in Table 2. From an average of these values a linear interpolation procedure is carried out over the central line band. This linearly interpolated flux is then connected piecewise with the average fluxes of the red and blue sidebands, and a robust fit is performed over the entire region of the blue sideband + line band + red sideband to derive the final local continuum estimate.

## 3.2. Measurement of Line Indices

Line indices (or equivalent widths) are calculated by integrating a continuum normalized flux over the specified wavelength regions of each line band. Two different measurements of line indices, obtained from the two different continuum methods described above, are reported, even though the line-index based methods for stellar parameter estimates only make use of the local continuum-based indices. In order to avoid spurious values for the derived indices, if a given index measurement is greater than $100\,\text{Å}$, or is negative, we set the reported value to $-9.999$. No parameter estimates based on that particular line index are estimated.

Table 2 lists the complete set of line indices made use of by the SSPP. Note that, unlike the case for most of the features in this Table, the line indices listed in rows 74 (TiO1), 75 (TiO2), 76 (TiO3), 77 (TiO4), 78 (TiO5), 79 (CaH1), 80 (CaH2), 81 (CaH3), 82 (CaOH), and

83 (H$\alpha$) are calculated following the prescription given by the "Hammer" program (Covey et al. 2007). The line index for Ca I at 4227 Å and the Mg I$b$ and MgH features around 5170 Å are computed following Morrison et al. (2003), so that they might be used to estimate log $g$, as described in §4.4.

We follow the Cayrel (1988) procedure to compute an error for each line index measurement. The uncertainty ($W_{error}$) in the index or measured equivalent width is:

$$W_{error} = \frac{1.6 \times (resolution \times pixel\ size)^{1/2}}{SNR} \tag{1}$$

where $SNR$ is the signal-to-noise ratio in the local region of the spectrum, the *resolution* is taken to be $\sim 2.5$ Å, and the *pixel size* is set to 1 Å for the blue region (3800−6000 Å) and 1.5 Å for the red region (6000−9000 Å). The noise spectrum provided by the SDSS spectroscopic reduction procedure is used to compute the local $SNR$.

## 4. Methodology

The SSPP employs a number of methods for estimation of effective temperature, surface gravity, and metallicity based on SDSS spectroscopy and photometry. In this section the methods used in the SSPP are summarized. Since many of the methods implemented in the SSPP are already described by previously published papers, we will address those techniques briefly, and refer the reader to individual papers for detailed descriptions. The methods that are introduced here for the first time are explained in more detail. Note that some approaches derive all three atmospheric parameters simultaneously, while others are specific to an individual parameter.

### 4.1. Spectral Fitting With the k24 and ki13 Grids

These two methods are based on identification of the parameters for a model atmosphere that best matches the observed fluxes in a selected wavelength interval, as described in detail by Allende Prieto et al. (2006). Classical LTE line-blanketed model atmospheres are used to compute a discrete grid of fluxes, and interpolation allows sub-grid resolution. The search is performed using the Nelder-Mead algorithm (Nelder & Mead 1965).

The same grid described by Allende Prieto et al. (2006) is used by the SSPP. We refer to this set of model fluxes as the k24 grid. It includes a predicted broadband color index

$(g - r)$, as well as normalized spectral fluxes in the region $4400-5500$ Å at a resolving power of $R = 1000$. Kurucz (1993) model atmospheres and simplified continuum opacities are used to calculate synthetic spectra. The broadband photometry was derived from the spectral energy distributions provided by Kurucz (1993), passbands for point sources determined by Strauss & Gunn (2001), and an assumed airmass of 1.3.

In addition to the k24 grid, a second grid, referred to as ki13, is now implemented in the SSPP. This second grid covers the same spectral window as k24, but no photometry is considered. The use of only the derived normalized spectra de-couples the results based on this grid from reddening and photometric errors, although valuable information, mainly on the effective temperature, is sacrificed.

There are several other differences between the k24 and ki13 grids. The new grid includes molecular line opacities, with the most relevant molecules in the range of interest being the CH G-band near $4300$ Å as well as the MgH band. In addition, the ki13 grid takes advantage of a novel concept that allows for a significant increase in the speed of the calculation of model fluxes. The relevant opacities are not calculated for all depths in all models, but instead are obtained on a temperature and density grid, and later interpolated to the exact points in any given model atmosphere (Koesterke et al. 2007). The opacity grid includes 4 points per decade in density and steps of 125 K in temperature. With these choices, linear interpolation leads to errors in the derived normalized fluxes smaller than 1%.

Allende Prieto et al. (2006) made use of several libraries of observed spectra and atmospheric parameters to study systematic and random errors obtained from the k24 analysis. Even at infinite signal-to-noise ratios, random errors appear significantly larger than systematic errors, and amount to 3% in $T_{\rm eff}$, 0.3 dex in $\log g$, and 0.2 dex in [Fe/H]. This is most likely the result of over-simplified model fluxes with a solar-scaled abundance pattern (including an enhancement of the $\alpha$ elements at low iron abundance), which is too limited to account for the chemical spread in real stars. The new ki13 grid offers a significant improvement in random errors, which at high signal-to-noise amount to 2 % in $T_{\rm eff}$, 0.2 dex in $\log g$, and 0.1 dex in [Fe/H], but a less robust behavior (due to the lack of color information) at low signal-to-noise ratios. Small systematic offsets in ki13 detected from the analysis of the spectra in the Elodie library (Prugniel & Soubiran 2001) are corrected using linear transformations.

As discussed in Allende Prieto et al. (2006), the k24 and ki13 approaches perform best in the range 5000 K $\leq T_{\rm eff} \leq$ 7000 K, which corresponds to $0.1 \leq g - r \leq 0.7$; the SSPP restricts the adopted parameters from these methods to this color range. These methods are designated in the SSPP according to the following: the $T_{\rm eff}$, $\log g$, and [Fe/H] estimated with the k24 are referred to as T9, G7, and M8, respectively, while these parameters estimated

from the `ki13` grid are referred to as T10, G8, and M9, respectively.

## 4.2. The Ca II K and Auto-Correlation Function Methods

These methods are based on the procedures outlined by Beers et al. (1999), where the interested reader should look for more details. A brief summary follows.

The Ca II K method makes use of a "band-switched" estimate of the pseudo-equivalent of the Ca II K line at 3933 Å, in combination with an estimate of a broadband color, to obtain a prediction of the [Fe/H] for a given star. The approach has been used for two decades during the course of the HK (Beers, Preston, & Shectman 1985, 1992) and the Hamburg/ESO objective prism surveys (Reimers & Wisotzki 1997; Christlieb 2003) for the determination of metallicities of stars with available medium-resolution (2–3 Å resolution, similar to the resolution of the SDSS spectra) follow-up spectroscopy. The original calibration is based on high-resolution abundance determinations (and $B - V$ colors) for a sample of $\sim 500$ stars. It is clear that one adopts the assumption that the calcium abundance tracks the iron abundance in a monotonic fashion, which is almost always valid. In the process of deriving the estimate of [Fe/H], the relationship between [Fe/H] and [Ca/Fe] used is as follows:

$$[\text{Ca/Fe}] = \begin{cases} 0 & \text{if } [\text{Fe/H}] \geq 0 \\ -0.267 \times [\text{Fe/H}] & \text{if } -1.5 \leq [\text{Fe/H}] < 0 \\ +0.4 & \text{if } [\text{Fe/H}] < -1.5 \end{cases} \qquad (2)$$

This method has been shown to perform well over a wide range of metallicities, in particular for stars with [Fe/H] $< -1.0$; external errors from the calibration indicate that it has an intrinsic error no greater than 0.15–0.20 dex in the color range $0.3 \leq B - V \leq 1.2$. Above [Fe/H] $= -1.0$, and in particular for cooler stars (below $T_{\text{eff}} = 5000$ K), the Ca II K line gradually begins to saturate. As a result, for cool, metal-rich stars, the method will generally return an estimate of [Fe/H] that is on the order of 0.5 dex too low. This is ameliorated somewhat by empirical corrections that are built into the program used to calculated this estimate, but it remains a source of concern. It is important to recognize that for stars with very low metallicities, and for warmer stars in particular, the Ca II K line is one of the few (in some cases only) metallic lines available in medium-resolution spectra. Hence, this estimator plays an especially important role in such situations.

Clearly, in the present application, a measurement of $B - V$ is not available. Hence, we used the observed (or predicted, when necessary) $g - r$ color to estimate the $B - V$ color. In order to accomplish this task, we made use of several hundred stars with existing $B - V$

colors obtained during the course of the HK and Hamburg/ESO surveys that happened to fall in the SDSS footprint, and as a result, had available $g - r$ colors (note that only the fainter, non-saturated stars could be used). These stars covered a variety of metallicities, but in particular a large number of stars with [Fe/H] $< -1.0$ were included. An approximate transformation, suitable for low-metallicity stars, was obtained by Zhao & Newberg (2006); the transform $B - V = 0.187 + 0.916(g - r)$ was employed. We plan on deriving a new calibration of this method, using $g - r$ colors directly, based on the large set of high-resolution observations of stars that are being obtained at present. This will eliminate the uncertainty inherent in the application of an approximate color transformation.

Comparison of the metallicities obtained from this method with those derived from high-resolution spectroscopy of SDSS-I/SEGUE stars, and for member stars of open and globular clusters with known [Fe/H], indicates that [Fe/H] for stars with $g - r > 0.7$ are consistently underestimated (due to saturation of the Ca II K line); we consider only metallicities determined for stars with $0.1 \leq g - r \leq 0.7$ as valid estimates from this approach.

The auto-correlation function technique was developed as an alternative method for metallicity estimation which should perform well at higher metallicities, where the Ca II K technique is limited by saturation. As described in Beers et al. (1999), and references therein, the method relies on an auto-correlation of a given stellar spectrum, which generates a correlation peak whose strength is proportional to the frequency and strength of weak metallic lines in a given spectrum. The more such lines exist, the stronger the signal. This function has been calibrated as a function of $B - V$ color; as before, a transformation from $g - r$ to $B - V$ is used in order to obtain a prediction of [Fe/H].

The auto-correlation signal is expected to depend strongly on the signal-to-noise of a given spectrum, growing with decreasing $S/N$. Essentially, in the low $S/N$ limit, this function is responding to noise peaks rather than to the presence of metallic features. This effect can be corrected for – the measured $S/N$ over the region in which the auto-correlation function is calculated enters as a part of the calibration, and is effectively subtracted off. We performed such a procedure for a set of SDSS stellar spectra with parameters obtained from an early version of the SSPP. While the auto-correlation function method exhibits a rather small star-to-star abundance scatter when applied to the spectra of stars from open and globular clusters of known metallicity (indicating that it is performing well), it suffers a significant metallicity offset (0.5 to 1.0 dex too low), suggesting that the initial calibration to the SSPP was suspect. Although we calculate the value of this function during the execution of the SSPP, we do not employ it in the final derived abundance estimates. In the near future, we expect to obtain a re-calibration of this approach, based on the high-resolution spectroscopic observations that have now been carried out. This re-calibration

will also be performed directly to $g - r$ colors.

The [Fe/H] estimates from these two approaches are referred to as M4 for the Ca II K method, and as M5 for the auto-correlation function technique.

### 4.3. Calibration of a Ca II Triplet Estimator of Metallicity

The SDSS spectra extend to sufficiently red wavelengths to include the prominent Ca II triplet feature, which covers a spectral region $8400-8700\,\text{Å}$. These lines are known to be sensitive to both luminosity (surface gravity) as well as metallicity, so care must be exercised in their use as a metallicity indicator.

We have employed a line index that measures the integrated strength of these lines, corrected for the presence of Paschen H lines, which also occur in this wavelength interval. The line index definition, and the calculation of the summed index, is as described by Cenarro et al. (2001a,b). In order to calibrate this index for use with SDSS spectra, we have taken the library of some 700 spectra (and their listed atmospheric parameters) given by Cenarro et al. (see http: //www.ucm.es/info/Astrof/ellipt/CATRIPLET.html), rebinned the spectra to the SDSS spectral resolution, and calculated the corrected Ca II triplet index. This index, along with their listed de-reddened value of the $B - V$ color, are used as inputs to an artificial neural network procedure in order to predict the estimated [Fe/H]. This procedure is able to reproduce the metallicity of the Cenarro et al. stars to within $\pm 0.3$ dex over the temperature range 4000 K to 8000 K, with some residual sensitivity to surface gravity.

After significant testing, it was decided that the SDSS spectra in the regions of the Ca II triplet suffered from too much noise (often due to poor sky subtraction) in this region in order for this approach to be implemented in the present SSPP. However, we are now mounting a new effort to better clean the Ca II triplet region of residual sky noise in order to see if this indicator can be salvaged. The [Fe/H] estimated from this method is referred to as M6.

### 4.4. Calibration of a Gravity Estimator Based on the Ca I (4227 Å) and Mg I $b$ and MgH Features

Among the prominent metallic species in stellar spectra, the two that are most sensitive to surface gravity are the Ca I line at $4227\,\text{Å}$ and the Mg I $b$ and MgH features around $5170\,\text{Å}$. Both of these lines exhibit sensitivity to metallicity as well. We have adopted the line index measurements and quoted atmospheric estimates of [Fe/H] for the dwarfs and

giants in the calibration sample of Morrison et al. (2003), which were measured at a similar spectral resolution to the SDSS ($2.5-3.5\,\text{Å}$). Surface gravity estimates for the stars involved in this calibration were obtained from the compilation of Cayrel de Strobel (2001), while $B - V$ colors were obtained from the SIMBAD database.

These indices, along with their de-reddened $B - V$ colors and [Fe/H], are used as inputs to an artificial neural network procedure in order to predict the estimated surface gravity $\log g$. This procedure indicates that the prediction errors of the surface gravity, based on the Ca I and MgH indices are on the order of 0.35 dex and 0.30 dex, respectively.

As indicated by Morrison et al. (2003), these two methods are valid in the color range corresponding to $0.4 \leq g - r \leq 0.9$. The gravity estimated from Ca I is referred to G4, while that obtained from the MgH feature is referred to as G5.

## 4.5.   Parameters Obtained from the Wilhelm et al. (1999) Procedures

These methods are based on the routines described by Wilhelm, Beers, & Gray (1999; WBG99), to which we refer the interested reader. Extensions of these methods used in the SSPP are described below.

The procedures implemented in the SSPP are optimized for two separate temperature ranges, one for the warmer stars ($g-r \leq 0.25$), and one for the cooler stars with redder colors than this limit. The stellar parameter determinations make use of comparisons to theoretical $ugr$ colors and line parameters from synthetic spectra, both generated from ATLAS9 model atmospheres (Kurucz 1993). The synthetic spectra used in these procedures were generated using the spectral synthesis routine SPECTRUM (Gray & Corbally 1994).

For the hotter stars, the observed normalized spectra are fit with a Voigt profile to determine the Balmer-line equivalent widths and the $D_{0.2}$ (the line width at 20% below the local pseudo-continuum level) widths for H$\delta$, H$\gamma$, and H$\beta$. The combination of Balmer-line equivalent widths, $D_{0.2}$, and $u - g$ and $g - r$ colors are used to establish initial $T_{\text{eff}}$ and $\log g$ estimates, computed from functional trends in the theoretical model parameters. For stars cooler than $T_{\text{eff}} \sim 8000$ K, the surface gravity is mainly determined by the $u - g$ color. For hotter stars the surface gravity is primarily determined by the $D_{0.2}$ parameter. A metallicity estimate is determined through the use of a combination of the equivalent width of the Ca II K line and a comparison to synthetic spectral regions that contain other metallic lines. Once an initial abundance is established, the procedure is iterated to convergence in all three stellar parameters.

For the cooler stars, only the $g - r$ color is used to establish an initial estimate of $T_{\text{eff}}$. For these stars, $\log g$ is determined from the $u - g$ color for stars as cool as $T_{\text{eff}} = 5750$ K. For stars cooler than this limit, the strength of MgH is compared to synthetic spectra of similar $T_{\text{eff}}$ and [Fe/H] through the use of a band-strength indicator. The metal abundance is determined by the combination of the Ca II K line strength and a minimum $\chi^2$ comparison to metallic-line regions in the spectra. The procedure is then iterated to convergence.

For stars with $S/N > 10/1$, errors on the order of $\sigma(T_{\text{eff}}) = 225$ K, $\sigma(\log g) = 0.25$ dex, and $\sigma([\text{Fe/H}]) = 0.3$ dex can be achieved with this technique. The color range of $g - r$ over which this approach is used for the SSPP is $-0.2 \leq g - r \leq 0.8$. The effective temperature, surface gravity, and [Fe/H] estimated from this technique are referred to as T8, G6, and M7, respectively.

## 4.6.  The Neural Network Approach

The SSPP implements a flexible method of regression that provides a global non-linear mapping between a set of inputs (the stellar spectrum $\mathbf{x}_i$) and a set of outputs (the stellar atmospheric parameters, $\mathbf{s} = \{T_{\text{eff}}, \log g, [\text{Fe/H}]\}$). This method has been described in detail by Re Fiorentin et al. (2007), to which the interested reader is referred for more details.

For the present application, it should be noted that we have chosen not to include input photometry, although this certainly could be added if desired. We build an RR regression model (which means we are training the approach based on real, as opposed to synthetic, spectra) to parameterize real spectra. The training and evaluation data sets are taken from a set of 38,731 stars from 140 SEGUE plates, in directions of low reddening, which have had atmospheric parameters estimated by a preliminary version of the SSPP. This step, which one might think of as "internal training," is clearly not optimal, as one would ideally like an independent basis for the training. This was not possible, until recently, due to the absence of an adequate noise model for SDSS spectra. Such a model has now been developed; we are in the process of testing and evaluation of its use in combination with a new grid of synthetic spectra, and anticipate implementing it in future versions of the neural network approach.

Figure 3 compares our model estimates with those from the early version of the SSPP on the evaluation set. Overall we see good consistency, especially for stars with $T_{\text{eff}} < 8000$ K ($\log T_{\text{eff}} = 3.90$). Above this effective temperature our models underestimate $\log T_{\text{eff}}$ relative to the SSPP. Most regression models such as ours are designed to interpolate, rather than extrapolate. Extrapolation of the model to estimate atmospheric parameters that are not spanned by the training set is relatively unconstrained. Furthermore, the accuracy of the

RR model is limited by the accuracy of the target atmospheric parameters used in training, as well as their consistency across the parameter space. In this case, the SSPP estimates are combinations from several estimation models, each of which operates only over a limited parameter range. Thus, the transition we see above 8000 K may indicate a temperature region where one of the SSPP sub-models is dominating the SSPP estimates, and this is not well-generalized by our model. From this comparison, we find that the accuracies of our predictions (mean absolute errors) for each parameter are $\sigma(T_{\text{eff}}) = 170$ K, $\sigma(\log g) = 0.36$ dex, and $\sigma([\text{Fe/H}]) = 0.19$ dex.

The RR model has the advantage that exactly the same type of data are used in the training and application phases, thus eliminating the issue of discrepancies in the flux calibration or cosmic variance of the two samples. Of course, this requires an independent estimation method ("basis parameterizer") to parameterize the training templates (which itself must use synthetic models at some level). Our regression model then automates and – more importantly – generalizes this basis parameterizer. Indeed, the basis parameterizer may even comprise multiple algorithms, perhaps operating over different parameters ranges or used in a voting system to estimate atmospheric parameters. This is true in the present case, where the basis parameterizer comes from a preliminary version of the SSPP.

Experience with the behavior of the neural network approach on the SDSS-I/SEGUE data indicated that this method tends to underestimate [Fe/H] below $T_{\text{eff}} = 5000$ K and above $T_{\text{eff}} = 7500$ K, so we restrict its application to this range of temperature, which corresponds to $0.1 \leq g - r \leq 0.7$. Estimates of $T_{\text{eff}}$, $\log g$, and [Fe/H] obtained from the neural network approach are referred to as T7, G3, and M3, respectively.

## 4.7. The $\chi^2$ Minimization Technique Using the `NGS1` and `NGS2` Grids

### 4.7.1. Grids of Synthetic Spectra

We have made use of Kurucz's NEWODF models (Castelli & Kurucz 2003), which employ solar relative abundances from Grevesse & Sauval (1998), to generate two sets of grids of synthetic spectra. The model atmospheres assume plane-parallel line-blanketed model structures in one-dimensional local thermodynamical equilibrium (LTE), and an enhancement of alpha-element abundances by +0.4 dex for stars with [Fe/H] $\leq -0.5$. These new models include $H_2O$ opacities, an improved set of TiO lines, and no convective overshoot (Castelli, Gratton, & Kurucz 1997).

For production of the synthetic spectra we employed the `turbospectrum` synthesis code (Alvarez & Plez 1998), with solar abundances by Asplund, Grevesse & Sauval (2005), which

uses the treatment of line broadening described by Barklem & O'Mara (1998). The sources of atomic lines used by turbospectrum come from largely the VALD database (Kupka et al. 1999). Linelists for the molecular species CH, CN, OH, TiO, and CaH are provided by B. Plez (see Plez & Cohen 2005, private communication), while the lines of NH, MgH, and the $C_2$ molecules are adopted from the Kurucz line lists (see http: //kurucz.harvard.edu/LINELISTS/LINESMOL/). The grid of the synthetic spectra produced has resolutions of 0.01 Å or 0.005 Å, and spans from 3500 K $\leq T_{\mathrm{eff}} \leq$ 10,000 K in steps of 250 K, $0.0 \leq \log g \leq 5.0$ in steps of 0.25 dex, and $-4.0 \leq$ [Fe/H] $\leq +0.5$ in steps of 0.25 dex. These synthetic spectra are referred to as the NGS1 grid. After their generation, these synthetic spectra were degraded to the SDSS resolution $R = 2000$, using a Gaussian convolution algorithm, then sampled into 1 Å per pixel for application of the spectral matching technique described below.

A second grid of model atmospheres was constructed from the Kurucz ATLAS9 models (Castelli & Kurucz 2003), which do not employ alpha-element enhancements for models with [Fe/H] $\leq -0.5$. The turbospectrum synthesis code was again used to generate the synthetic spectra. The synthetic spectra have a resolution of 0.1 Å, and cover 4000 K $\leq T_{\mathrm{eff}} \leq$ 8000 K in steps of 250 K, $0.0 \leq \log g \leq 5.0$ in steps of 0.25 dex, and $-3.0 \leq$ [Fe/H] $\leq$ $+0.5$ in steps of 0.25 dex. Ranges in [$\alpha$/Fe] were introduced for spectral synthesis, over $-0.2 \leq$ [$\alpha$/Fe] $\leq +0.8$, in steps of 0.2 dex for each value of $T_{\mathrm{eff}}$, $\log g$, and [Fe/H]. These synthetic spectra are referred to as the NGS2 grid. After their generation, these synthetic spectra are also smoothed to the resolution of the SDSS spectrographs. The primary purpose of creating the NGS2 grid is to enable (future) methods for the determination of [$\alpha$/Fe] for stars in the range 4000 K $\leq T_{\mathrm{eff}} \leq$ 8000 K. However, since this is an independent grid, it is also possible to obtain another set of predicted stellar atmospheric parameters for the stars within this temperature range.

### 4.7.2. Pre-processing Observed Spectra for the $\chi^2$ Minimization Technique

The observed SDSS spectra are processed as described in §3 above. The blue region of the spectrum contains most of the information required to constrain the stellar parameters, but for cooler stars, the observed signal-to-noise ratio peaks in the red region. As a compromise, and in order to speed up the analysis, we only consider the spectral range 4500−5500 Å. The spectrum under consideration is normalized after obtaining a pseudo continuum over the 4500−5500 Å range. The continuum fit is carried out in a similar fashion to that described in §3, but lower (third and fourth) order polynomials are employed, due to the shorter wavelength coverage. The synthetic spectra that are used to match with the

observed spectra are also normalized in the same fashion over the same wavelength range.

### 4.7.3. The Parameter Search Technique

Foloowing the above steps, we then carry out a search for the best-fit model parameters, i.e., those that minimize the difference between the observed flux vector, $O$, and the synthetic flux vector, $S$, as functions of $T_{\mathrm{eff}}$, $\log g$, and [Fe/H] using a reduced $\chi^2$ criterion. That is,

$$\chi^2/DOF = \sum_{i=1}^{m+1} (O_i - S_i)^2/\sigma_i^2, \tag{3}$$

where $\sigma_i$ is the error in flux in the $i$th pixel.

To reduce the number of model spectra that must be considered in the calculation of the the reduced $\chi^2$ values, we first obtain an approximate effective temperature based on a simple approximation. This procedure, which is referred to as the Half Power Point (HPP) method (Wisotzki et al. 2000), obtains an estimate of the wavelength at which the total integrated flux over a spectrum is equal to half of the flux obtained over the entire wavelength region (in this case we use $3900-8000\,\text{Å}$). Since the flux distribution for a given stellar spectrum varies strongly with effective temperature, once we have determined the HPP wavelength, we are able to obtain a reasonably accurate estimate of effective temperature (or a broadband color such as $g - r$) by comparing with the HPP wavelengths obtained from a grid of synthetic spectra. The relation between effective temperature and HPP wavelength is established by fitting a polynomial:

$$T_{\mathrm{eff}} = (25.63 - 114.51\mathrm{HPP} + 177.17\mathrm{HPP}^2 - 93.55\mathrm{HPP}^3) \times 10,000 \text{ K}, \tag{4}$$

where, HPP = wavelength/10,000.

We initially select synthetic spectra over a broad range around this predicted effective temperature, within $\pm 1500$ K. For example, if the HPP predicted temperature of a star is 5000 K, we consider models between 3500 K and 6500 K. As long as the observed spectrum doesn't have a grossly incorrect spectrophotometric calibration, the estimated temperature will be well within this range. We then obtain the reduced $\chi^2$ values between the observed and the selected synthetic spectra over a $4500-5500\,\text{Å}$ wavelength window.

Considering the distribution of reduced $\chi^2$ values as a function of effective temperature only, we now have 399 points (21 different gravities and 19 metallicities) in each temperature

grid. We then iteratively clip, in each temperature grid, points that have larger values of reduced $\chi^2$ than the median of the reduced $\chi^2$ values in each temperature grid. This iterative procedure is performed five times, with the clipped values being those that are higher than the median of all surviving values in each step. After this, only a few points in each temperature step are left. Figure 4 shows one example of the result of this procedure. We then fit the reduced $\chi^2$ distribution to a fourth-order polynomial function as a function of temperature. At this point, we clip off any points that lie farther than $2\sigma$ below and $1\sigma$ above the fitted curve. In this manner, we are able to easily find the likely global minimum, instead of becoming stuck in an spurious local minimum. The adopted effective temperature is taken as the minimum of this fit (shown as the red line in Figure 4).

Once the effective temperature is determined, we are able to narrow down the model grids further. To obtain estimates of [Fe/H] and log $g$, we select models within $\pm550$ K of the estimated $T_{\mathrm{eff}}$, and then exploit the same iterative procedure as above. Note that the values of reduced $\chi^2$ respond sensitively to small changes in $T_{\mathrm{eff}}$ and [Fe/H], allowing for their optimal determinations. However, variations in the log $g$ values do not strongly impact the reduced $\chi^2$, due to a shortage of gravity-sensitive lines in the spectral window we examine. This leads to potentially large errors in the estimated log $g$. These procedures are applied to both the NGS1 and NGS2 grids.

Figure 5 shows two examples of synthetic spectra with parameters set to those estimated by the procedure described above, over-plotted on the observed spectral data. The $T_{\mathrm{eff}}$, log $g$, and [Fe/H] estimated from NGS1 are referred to as T6, G2, and M2, respectively, while the log $g$ and [Fe/H] estimated from NGS2 are referred to as G1 and M1, respectively. No independent estimate of $T_{\mathrm{eff}}$ is obtained from the NGS2 grid, as it is essentially degenerate with that determined from the NGS1 grid.

### 4.7.4. Comparisons with Spectral Libraries and Analysis of High-Resolution SDSS-I/SEGUE Stars

In order to validate that the NGS1 and NGS2 grid approaches perform well in determining stellar parameter estimates, we compare the results from these techniques with literature values from two spectral libraries: ELODIE (Prugniel & Soubiran 2001; Moultaka et al. 2004) and MILES (Sánchez-Blázquez et al. 2006), and with those derived from analysis of the SDSS-I/SEGUE stars with available high-resolution spectroscopy.

*Validation from the ELODIE and MILES Spectral Libraries*

The spectra in the ELODIE library were obtained with the ELODIE spectrograph at the Observatoire de Haute-Provence 1.93 m telescope, and cover the spectral region $4000-6800$ Å. We employ 1969 spectra of 1390 stars with a resolving power $R = 10,000$, which are publicly available as part of the ELODIE 3 release (Moultaka et al. 2004). The spectra are first smoothed with a Gaussian kernel to match the SDSS resolution. Most of the spectra have quite high $S/N$ ratios, and are accompanied with estimated stellar parameters from the literature. Each spectrum (and parameter estimate) has a quality flag ranging from 0 to 4, with 4 being best. In our comparison exercise, we only select stars with 4000 K $\leq T_{\text{eff}} \leq$ 10,000 K with a quality flag $\geq 1$ for the spectra and all of the parameters.

Our examination indicates that these two approaches work best in the range 5000 K $\leq$ $T_{\text{eff}} \leq 8000$ K. Comparison plots between the literature values and the estimated parameters in this temperature range for 562 stars among the ELODIE spectral library are shown in Figure 6. A Gaussian fit to the residuals of each parameter reveals that the NGS1 estimate of $T_{\text{eff}}$ is higher by 86 K ($\sigma = 96$ K), the surface gravity is larger by 0.10 dex ($\sigma = 0.24$ dex ), and the metallicity is smaller by 0.17 dex ($\sigma = 0.14$ dex), on average. For cooler stars, with 4000 K $\leq T_{\text{eff}} \leq 5000$ K, we find that $< \Delta(T_{\text{eff}}) >$ and $< \Delta([\text{Fe/H}]) >$ are 177 K ($\sigma = 145$ K) and 0.09 dex ($\sigma = 0.20$ dex), respectively, which are relatively small offsets and scatter, while the $< \Delta(\log g) >$ is 0.48 dex with $\sigma = 0.36$ dex.

Because the spectra from the ELODIE library are of very high quality, one might wonder how the parameter estimates would compare for the lower $S/N$ data included among the SDSS-I/SEGUE stars. In order to test this, we inject Gaussian noise into the ELODIE spectra to force them to $S/N = 50/1$, $25/1$, $12.5/1$, and $6.25/1$ per pixel at 5000 Å, respectively, degrade them to the SDSS resolution, and apply the same procedures as above for estimation of the stellar atmospheric parameters. These test spectra, and more detailed information on noise models can be found in ftp://hebe.as.utexas.edu/pub/callende/sdssim/. Table 3 shows the results of this exercise. Inspection of this Table shows that, for $S/N \geq 12.5/1$, the shifts and scatter in the determinations of the parameters remain acceptably small.

The MILES library includes 985 spectra obtained with the 2.5m INT and the IDS spectrograph at La Palma. The wavelength coverage is $3530-7430$ Å, and the resolution is $\sim 2.3$ Å (Sánchez-Blázquez et al. 2006). Because the resolution of the spectra is similar to that of SDSS spectra, we make use of the original MILES spectra in the analysis. After dropping the spectra with missing parameters, and outside the temperature range 5000 K $\leq T_{\text{eff}} \leq 8000$ K, 367 spectra remain. Figure 7 shows the comparison plots between the selected literature values and the parameters estimated from NGS1 procedure. It is clear from this Figure that offsets and scatter for the three atmospheric parameters are very close

to those obtained by comparison with the ELODIE spectral library. For the cooler stars, with $4000$ K $\leq T_{\text{eff}} \leq 5000$ K, we obtain $< \Delta(T_{\text{eff}}) > = 179$ K with $\sigma = 133$ K, $< \Delta([\text{Fe/H}]) > = 0.06$ dex with $\sigma = 0.17$ dex, and $< \Delta(\log g) > = 0.58$ dex with $\sigma = 0.45$ dex.

Very similar behaviors were found for comparison of the NGS2 grid technique as for the NGS1 grid technique. Table 3 summarizes the offsets between the literature values and the estimated parameters for both synthetic grid approaches.

We conclude from these comparisons that estimates of $T_{\text{eff}}$ and [Fe/H] over $4000$ K $\leq T_{\text{eff}} \leq 8000$ $K$ (corresponding to $0.0 \leq g - r \leq 1.2$) should be acceptable. Surface gravity estimates from these techniques are sufficiently accurate over $5000$ K $\leq T_{\text{eff}} \leq 8000$ K (corresponding to $0.0 \leq g - r \leq 0.7$) for both synthetic grid approaches. Both approaches require that, in order to obtain useful parameter estimates, the $S/N$ ratio of the spectra should be larger than $S/N = 12.5/1$; for the purpose of the SSPP we conservatively adopt $S/N \geq 20/1$ in the color range $0.0 \leq g - r \leq 0.4$, and $S/N \geq 10/1$ in the color range $0.4 \leq g - r \leq 1.2$.

*Validation from SDSS-I/SEGUE Stars with Available High-Resolution Spectra*

As part of a long-term program to validate and improve estimates of stellar atmospheric parameters determined by the SSPP, over the past two years we have obtained higher resolution spectra for over 150 SDSS-I and SEGUE stars. The targets cover a wide range of temperature and metallicity, but somewhat less so in surface gravity. Existing "holes" in the parameter space will be given high priority for future high-resolution campaigns. The data have been independently reduced and analyzed by two authors (C.A. and T.S.). For a detailed description of these analyses, the interested reader is referred to Paper III. Among this sample, we selected 124 stars which have single-lined spectra, $S/N > 40/1$ per pixel at 6000 Å, and with well-determined stellar parameters. For simplicity of our present comparison, we adopt the mean values of stellar atmospheric parameters obtained by the independent analysis efforts.

Figure 8 shows a comparison between the parameters estimated from the NGS1 grid approach and those determined from high-resolution analysis, over $5000$ K $\leq T_{\text{eff}} \leq 8000$ K. As summarized in Table 3, unlike for the comparisons with the spectral libraries, the temperature and surface gravity estimates obtained from NGS1 present negligible zero-point offsets, $5$ K ($\sigma = 137$ K) and $0.00$ dex ($\sigma = 0.30$ dex) dex, respectively. The average metallicity offset ($-0.12$ dex) and scatter ($0.17$ dex) are very close to those obtained by comparison with the two libraries. Considering the results from these three different comparisons, a small systematic offset in our derived metallicities from this method may exist. However,

we don't adjust any of these offsets in the current SSPP. Adjustments will be considered for future refinements of the SSPP, once a significant number of additional high-resolution data for SDSS-I/SEGUE stars are obtained.

## 5. Empirical and Theoretical Predictions of $g - r$ Color and $T_{\text{eff}}$

### 5.1. Predictions of $g - r$ Color

For a variety of reasons (e.g., nascent saturation, difficulties with de-blending of sources, high reddening, etc.), the SDSS PHOTO pipeline (Lupton et al. 2001) occasionally reports incorrect, or less-than-optimal estimates of the broadband colors for a given target. Because several of the methods we employ in the SSPP require a good measurement of (at least) the $g - r$ color, it is useful to check if the reported $g - r$ color is commensurate with that predicted from the flux-calibrated spectrum of the source, or with the strength of spectral lines that correlate with effective temperature. This predicted color is used to raise a cautionary flag for stars with possibly incorrect reported colors, within some tolerance. We have developed three different methods to predict $g - r$ color in the SSPP, as described below.

#### 5.1.1. Prediction of $g - r$ Color from the Half Power Point Method

The first technique, the Half Power Point (HPP) method (Wisotzki et al. 2000), has been described in §4.7 above, in connection with refining grid searches of parameter space. Here we obtain an empirical calibration of the (de-reddened) $g - r$ by fitting a functional relationship between the HPP wavelength of spectra for stars with well-measured SDSS colors, and located in regions of high Galactic latitude, where reddening is minimal. The best-fit relationship is of the form:

$$g - r = -3.354 + 4.318\text{HPP} + 3.247\text{HPP}^2, \tag{5}$$

where HPP = wavelength/10,000. The expected error in prediction is about 0.08 magnitudes, over a broad range of color.

The predicted color obtained in this fashion is (obviously) also a way to identify stellar spectra with poor spectrophotometric flux calibrations. If the observed color reported by SDSS PHOTO is believed to be correct, and there remains a difference with the color obtained from the above relationship, one might be justifiably concerned about the quality of the

spectrophotometric correction that has been applied. Unresolved binaries, especially those involving a red and a blue member, can also be identified by looking for discrepancies between the observed and predicted $g - r$ colors.

### 5.1.2. Prediction of $g - r$ Color from the H$\delta$ and H$\alpha$ Lines

The strengths of the Balmer lines of hydrogen are also tightly correlated with $g - r$ color over wide ranges of effective temperature. We have made use of the line indices for H$\delta$ and H$\alpha$, as determined by the SSPP, to obtain the following relationships:

$$g - r = 0.469 - 0.058HD24 \tag{6}$$

and

$$g - r = 0.818 - 0.092HA24, \tag{7}$$

where $HD24$ and $HA24$ are the H$\delta$ and H$\alpha$ line indices calculated over a 24 Å band centered on these lines. Note that since the H$\alpha$ line is stronger, at a given color, than the H$\delta$ line, it can be used to determine predictions of colors for cooler stars. The H$\alpha$ line is also located in a region of the spectrum where one expects generally fewer problems with contamination of the index from nearby metallic features.

## 5.2. Predictions of $T_{\mathrm{eff}}$

Effective temperatures predicted by the observed $g - r$ color, or through the strength of the Balmer lines, are sufficiently accurate to be considered as auxiliary estimators to those methods described in §4. We obtain two theoretical and three empirical temperature estimates during execution of the SSPP.

### 5.2.1. Theoretical $T_{\mathrm{eff}}$ Estimates

Two theoretical temperature estimates are based on grids of synthetic spectra generated using the Kurucz models described above, and by consideration of predicted colors from the Girardi et al. (2004) isochrones. For the temperatures based on Kurucz models, we calculate

an estimated $g - r$ color, adopting the SDSS filter and instrumental response functions (Strauss & Gunn 2001), then fit a fourth-order polynomial:

$$T_{\text{eff}} = 7792.22 - 6586.18(g - r) - 4637.23(g - r)^2 - 1994.29(g - r)^3 - 386.24(g - r)^4 \quad (8)$$

In deriving the above relationship, we take into account stellar models with atmospheric parameters in the range $-2.0 \leq$ [Fe/H] $\leq -0.5$ and $3.0 \leq \log g \leq 5.0$, where most SDSS-I/SEGUE stars are found. Stars at the extrema of these ranges will have less than ideal estimates of temperature due to the sensitivity of $g - r$ color to either metallicity, surface gravity, or both. The effective temperature estimated from this relation is referred to as T3.

For the temperature estimates based on the Girardi et al. isochrones, we assume that the stars are all older than 10 Gyrs, are moderately metal poor (i.e., have metallicites in the range $-1.5 \leq$ [Fe/H] $\leq -0.5$), and are subgiants or main-sequence stars, which is true for a great majority of the SDSS-I/SEGUE stars. The relationship below, based on a third-order polynomial, is referred to as T4:

$$T_{\text{eff}} = 7590.26 - 6191.78(g - r) - 4270.92(g - r)^2 - 1225.12(g - r)^3 \quad (9)$$

### 5.2.2. Empirical $T_{\text{eff}}$ Estimates

Two of the three empirical temperature estimates we employ are derived from the Balmer-line strengths, similar to the color estimates discussed above, but calibrated to the effective temperature estimates obtained from the methods discussed in §4. The temperatures estimated from the $HA24$ and $HD24$ indices, via the simple linear relationships below, are referred to as T1 and T2, respectively.

$$T_{\text{eff}} = 4133 + 371HA24 \quad (10)$$

$$T_{\text{eff}} = 5449 + 206HD24 \quad (11)$$

We restrict the regions over which the above relationships are applied to $1.0\,\text{Å} \leq HA24 \leq 12.0\,\text{Å}$ and $1.0\,\text{Å} \leq HD24 \leq 15.0\,\text{Å}$, respectively.

The final empirical temperature estimate comes from the relationship between the effective temperature derived from a previous version of the SSPP and the observed $g - r$ color

(Ivezić et al. 2007). The temperature estimated from the relationship below is referred to as T5:

$$\log\ T_{\mathrm{eff}} = 3.8820 - 0.3160(g-r) + 0.0488(g-r)^2 + 0.0283(g-r)^3. \tag{12}$$

The above temperature estimates are taken into account by the SSPP provided that the color flag (see below) is not raised, and the expected temperature is beyond the region where the primary estimates derived from the techniques described in §4 apply. That is, they are used when the expected temperature is outside the range $4500\ \mathrm{K} \le T_{\mathrm{eff}} \le 7500\ \mathrm{K}$.

## 6. Flags Raised During Execution of the SSPP

It is important that the SSPP be able to identify situations where the quoted atmospheric parameters may be in doubt, or simply to make the user aware of possible anomalies that might apply to a given star. We have designed a number of flags which serve this purpose.

There are two primary categories of flags – critical flags and cautionary flags. When a critical flag is raised, the SSPP is set to either ignore the determinations of atmospheric parameters for a given star, or it is forced (in the case of the color flag described below) to take steps that differ from normal processing in an attempt to rescue this information. Obviously, even when information is salvaged, the presence of a critical flag means the user must be aware that special steps have been taken, and the reported estimated parameters must be viewed with this knowledge in mind. The second category of flags are the cautionary flags, which are provided for user consideration, but are not necessarily cause for undue concern. Indeed, sometimes these flags are raised when all is in fact OK, but the flag has been raised due to a peculiarity in the spectrum that is relatively harmless, and which will not unduly influence determination of atmospheric parameters. The user should nevertheless be aware of the existence of these flags.

The flags are combined into a single set of four letters, the meanings of which are summarized in Table 4, and described below in more detail. Four placeholders are used in order to accommodate cases where more than one sort of flag is raised.

The nominal condition for the four letter flag combination is 'nnnn', which indicates that the SSPP is satisfied that a given stellar spectrum (and its reported $g-r$ colors) has passed all of the tests that have been performed, and the stellar parameters should be considered well determined.

The first letter in this combination is set to one of 10 different values: 'n', 'D', 'd', 'H', 'h', 'l', 'E', 'S', 'V', and 'N'. Their explanations follow:

- 'n': The letter 'n' indicates nominal.

- 'D': The letter 'D' indicates that a comparison of the breadth of the H$\delta$ line at 20% below its continuum, $D_{0.2}$, and the line depth below the continuum, $R_c$, relative to their expected relationship for "normal stars", provided below, does not apply. The expected relationship is given by:

$$R_c = -0.009503 + 0.027740D_{0.2} - 0.000590D_{0.2}^2 + 0.000006D_{0.2}^3 \qquad (13)$$

  If $D_{0.2}$ is greater than 35.0 Å, and the predicted $R_c$ from the above relationship is less than the measured value, then the star is most likely a white dwarf. This is a critical flag.

- 'd': This flag is raised if $D_{0.2}$ is less than 35.0 Å, and the predicted $R_c$ from above is less than the measured value. In this case, the star is most likely a sdO or sdB star. This is a critical flag.

- 'H': This flag is raised when the estimated $T_{\rm eff}$ from the SSPP is greater than 10000 K, and is meant to indicate a hot star. This is a critical flag.

- 'h': This flag is raised if the estimated $T_{\rm eff}$ from the SSPP is greater than 8000 K, and either of the line indices of He I (at 4026.2 Å) or He I (at 4471.7 Å) is greater than 1.0 Å. This indicates that the star is likely to be a hot star. This is a critical flag.

- 'l': This flag is raised if the SSPP judges the star to have a high likelihood of being a late-type star (generally late K, M, or later spectral type), beyond the ability of the present pipeline to determine acceptable atmospheric parameter estimates. The condition used for raising the 'l' flag is that the Na line (5892.9 Å) index, as measured over a 24 Å band centered on this feature, is larger than 10 Å, and the $g - r$ color is greater than 0.80. This is a critical flag.

- 'E': This flag is raised if significant emission lines are detected in a spectrum. This is a critical flag.

- 'S': This flag is raised if the spectrum (according to the header information) is a night-sky spectrum. This is a critical flag.

- 'V': This flag is raised when an adequate radial velocity could not be found for a given spectrum. This is a critical flag.

- 'N': This flag is raised if the spectrum is considered noisy at the extremes of the wavelength range (e.g., around Ca II K and the Ca II triplet). This is a cautionary flag.

The flags that are used to fill out the remaining three positions of the four letter flag combination are 'C', 'B', 'G', or 'g', as described below:

- 'C': This flag is raised if the SSPP is concerned that the reported $g-r$ color is incorrect. As mentioned above, we calculate three estimates of predicted $g-r$ colors, based on $HA24$, $HD24$, or the Half Power Point method. For each of these three predicted colors, we find the one which is closest to the reported $g-r$ color based on the photometry. If the difference between the reported color and the closest predicted color is larger than 0.2 magnitudes, the color flag (C) is raised. The SSPP is set up to proceed with its calculations of atmospheric parameters using the predicted $g-r$ color. This flag is always found in the second position of the combination flag parameters. This is a critical flag.

- 'B': This flag is raised if the SSPP is concerned that there exists a strong mismatch between the strength of the predicted H$\alpha$ line index $HA24$, based on the measured H$\delta$ line index, $HD24$. For the great majority of "normal" stars, the predicted value of the H$\alpha$ line index is found to be $HA24 = 2.737 + 0.775HD24$. For stars with significant $HA24$ and $HD24$ measurements (which we take to mean that the values of these indices exceed zero by more than $2\sigma$, where $\sigma$ is the error in the measured line index), if the difference between the predicted $HA24$ line index and the measured $HA24$ index is larger than 2.5 Å, then the 'B' flag is raised. This flag is always found in the third position of the combination flag parameters. This is a cautionary flag.

- 'G or g': This flag is raised if the SSPP suggests that the star may exhibit a strong ('G') or mild ('g') CH G-band (around 4300 Å), relative to expectation for "normal" stars. This flag is always found in the fourth position of the combination flag parameters. This is a cautionary flag.

## 7.    The SSPP Decision Tree for Final Parameter Estimation

The SSPP uses multiple methods in order to obtain estimates of the atmospheric parameters for each star over a very wide range in parameter space. Each technique has limitations

as to its ability to estimate each parameter, arising from, e.g., the coverage of the grids of synthetic spectra, the methods used for spectral matching, and their sensitivity to the $S/N$ of the spectrum, the range in parameter space over which the particular calibration used for a given method extends, etc.. Hence, it is necessary to specify a prescription for the inclusion or exclusion of a given technique for the estimation of a given atmospheric parameter. At present, this is accomplished by the assignment of a null (0, meaning the parameter estimate is dropped), or unity (1, meaning the parameter estimate is accepted) value to an indicator variable associated with each parameter estimated by a given technique. In the future, we plan to devise an improved weighting scheme for the combinations of the parameter estimates, once the grid of high-resolution spectroscopic determinations of atmospheric parameters is more completely filled out.

The $S/N$ ratio of a given spectrum also plays a role in the final decision as to the estimate of a set of atmospheric parameters, and the techniques used (which differ in their sensitivity to $S/N$). Table 5 lists the ranges of $g - r$ and $S/N$ where each particular method is considered valid. Note that slightly higher requirements on $S/N$ presently exist for the bluer stars (those with $g - r < 0.3$) due to the inherent weakness of the metallic lines. We are presently exploring whether this requirement can be relaxed in the cases of several estimators. All derived parameters that fall outside of the color and $S/N$ ranges listed in this table, for a given technique, are set to $T_{\rm eff} = -9999$, $\log g = -9.999$, and $[{\rm Fe/H}] = -9.999$ by the SSPP.

Recall that in cases where the color flag 'C' is raised, the predicted $g-r$ color determined by the procedures described above is used as an input (rather than the reported color) for the techniques that require this information.

## 7.1. Decisions on Effective Temperature Estimates

There are five primary temperature estimates determined by the SSPP, and an auxiliary set of five empirically and theoretically determined estimates. Note that a few of the primary techniques extend to temperatures below 4500 K and above 7500 K, although the accuracy obtained by these are lower than in the interval 4500 K $< T_{\rm eff} <$ 7500 K. Thus, for stars with temperatures outside of this interval, we also include the auxiliary temperature estimates (in fact, just those that lie within $3\sigma$ of the mean of the full auxiliary set) in assembling the final average estimate of $T_{\rm eff}$.

In cases where the color flag 'C' is raised, we ignore all temperatures that rely on the reported $g - r$ color, and only consider those based on spectroscopy alone (e.g., the spectral

matching techniques). A robust average of the accepted temperature estimates (those with indicator variables equal to 1) is taken for the final adopted temperature. An internal robust estimate of the scatter around this value is also obtained.

## 7.2. Decisions on Surface Gravity Estimates

There are eight methods used to estimate surface gravity by the SSPP. Application of the limits on $g - r$ and $S/N$ eliminates a number of these estimates, and a robust average of the accepted log $g$ estimates (those with indicator variables equal to 1) is taken for the final adopted surface gravity. An internal robust estimate of the scatter around this value is also calculated.

## 7.3. Decisions on [Fe/H] Estimates

Nine different methods are employed to determine [Fe/H] in the present SSPP. As before, indicator variables of 1 or 0 are assigned to the result from each method, according to whether or not it satisfies the range of validity listed in Table 5. Note that two of the methods, the auto-correlation function technique (M5) and the Ca II triplet technique (M6) always have their indicator variables set to 0 at present, until better calibrations for these estimators can be obtained.

Three final values of [Fe/H] are determined from the assembled set of accepted estimators. These are referred to as the biweight[1] [Fe/H], the refined [Fe/H], and the adopted [Fe/H], as described below.

The biweight [Fe/H] is simply a robust average of all accepted estimates of metallicity with indicator variables equal to 1.

The refined [Fe/H] value is determined as follows. First, we select a small region of the (NGS1) grid where we find spectra that (globally) most closely match the adopted $T_{eff}$, the adopted log $g$, and the [Fe/H] from individual techniques with indicator variables equal to 1. As an example, if there exist five estimates of [Fe/H] (with indicator variables of 1, and using the adopted $T_{eff}$ and adopted log $g$), then five synthetic spectra with the same temperature and gravity, but five different metallicities, are selected. We then calculate reduced

---

[1]The biweight family of estimators smoothly diminish the effects of outliers on the resulting central location ("mean") and scale ("standard deviation"). See Beers, Flynn, & Gebhardt (1990) and references therein.

$\chi^2$ values in two restricted regions of wavelength space in the observed spectrum, relative to the selected synthetic spectra. The regions considered are the Ca II region $(3900-4000$ Å$)$ and the region surrounding the MgH feature $(5000-5500$ Å$)$. These two regions are selected because they retain the most sensitivity to metallicity for the extrema of the range of [Fe/H] and temperature encountered, i.e., for the most metal-poor/warm or metal-rich/cool stars. We then seek the best-matching synthetic spectrum over these regions alone, based on the minimum of reduced $\chi^2$ for both regions, respectively. This match is carried out independently for each region. Once the best matching synthetic spectrum (hence [Fe/H]) among the five selected synthetic spectra is identified, we select the accepted [Fe/H] estimates from the SSPP that lie within $\pm$ 0.15 dex of the [Fe/H] of the best-matching synthetic spectrum in each region. These are then averaged in order to obtain the best available metallicity estimate for each region. At this point we have two averaged estimates of [Fe/H], which may be the same (i.e., the same synthetic spectrum matches both regions equally well), or different.

If the adopted estimate of $T_{\mathrm{eff}} < 5300$ K , the refined [Fe/H] estimate is set to the average value obtained from the MgH region. The refined value is also set to the metallicity average obtained from this region for the case where $5300 \leq T_{\mathrm{eff}} \leq 6500$ K, and the biweight [Fe/H] is $> -1.2$. This value is also used when $T_{\mathrm{eff}} > 6500$ K and the biweight [Fe/H] is $\geq -0.8$.

The refined [Fe/H] is set to the average obtained for the Ca II region when $5300$ K $\leq T_{\mathrm{eff}}$ $\leq 6500$ K, and the biweight [Fe/H] is $\leq -1.2$. The refined value is also set to the metallicity average obtained from this region for the case where $T_{\mathrm{eff}} > 6500$ K and the biweight [Fe/H] is $< -0.8$.

The adopted [Fe/H] is then set as follows. If the difference between the biweight [Fe/H] and the refined [Fe/H] is less than 0.15 dex, the adopted [Fe/H] is set equal to the biweight [Fe/H]. If the difference exceeds 0.15 dex, the adopted [Fe/H] is set to the average value of the biweight [Fe/H] and the refined [Fe/H] estimators.

## 8. Validation of Final SSPP Parameter Estimates

We do not yet have at our disposal a completely satisfactory set of external spectral libraries, with suitable wavelength coverage and available atmospheric parameter estimates, that extends over the full range of parameter space explored by techniques employed by the SSPP. Hence, we are limited to comparison with the sets of parameters obtained from analysis of the high-resolution spectra for SDSS-I/SEGUE stars obtained to date, and with

information available from the literature for stars in Galactic open and globular clusters that have been observed during the course of the SDSS. We discuss these comparisons below.

## 8.1. Validation from High-Resolution Spectroscopy

Table 1 summarizes the high-resolution data for SDSS-I/SEGUE stars obtained to date. Although the stars in this Table cover most of the range explored by the SSPP techniques, there remain gaps in this coverage that we hope to fill in the near future.

As noted above, these data have been reduced and analyzed independently by two of the authors (C.A. and T.S.), making use of different methodologies. Details are discussed in Paper III. Tables 6, 7, and 8 summarize the systematic offsets and scatter obtained for estimates of $T_{\rm eff}$, log $g$, and [Fe/H] from each of the techniques used by the SSPP, relative to high-resolution analyses carried out individually, and collectively. The differences in the numbers of stars considered independently arises because T.S. (results shown as 'HA2' in the Tables) analyzed all available spectra, while C.A. (results shown as 'HA1' in the Tables) performed analysis only for those stars observed with the Hobby-Eberly Telescope (HET). In the analysis 'HA2', two different approaches were employed. The first is to use a routine for optimizing minimum distance. This method was employed for the HET and Keck-ESI spectra. The second is the traditional high-resolution analysis approach, using Fe I and Fe II lines to constrain $T_{\rm eff}$, log g$g$, [Fe/H], and microturbulence. This approach was applied to the Keck-HIRES and Subaru-HDS data. More detailed explanations on the methods can be found in Paper III. The Keck-ESI, Keck-HIRES, and Subaru-HDS spectra with available parameters are defined as 'OTHERS' in Paper III. It is noteworthy that in Paper III only HET data analyzed by C.A. are used to derive the empirical random errors of the SSPP. However, in this paper, we consider all available data with estimated parameters. The rows labeled 'MEAN' in Tables 6, 7, and 8 are the averaged results from HA1 and HA2 (for stars in common), supplemented with stars from HA2 where HA1 results were not obtained.

Figures 9, 10, and 11 provide comparisons of the estimates of atmospheric parameters for individual techniques used by the SSPP with those obtained from the high-resolution analysis, for $T_{\rm eff}$, log $g$, and [Fe/H], respectively. Note that comparisons are given even for the methods that are not fully implemented by the SSPP at present (e.g., the auto-correlation function and Ca II triplet metallicity estimators).

Comparison of the estimated temperatures from the SSPP indicates an overall very satisfactory result, although Table 6 reflects an interesting result for $T_{\rm eff}$; estimates are mostly higher for HA1 and mostly lower for HA2. However, as can also be noted from this

Table, the final adopted value of effective temperature from the SSPP exhibits a very small offset (+55 K), and a one-sigma scatter of 123 K, both of which are encouragingly small. It is clear from inspection of Figure 9 that additional high-resolution observations are required of stars with both higher and lower temperatures than the present sample. The distribution of the final adopted temperatures appears very well correlated with that of the mean values from the high-resolution analyses in the range of $4500 \text{ K} \leq T_{\text{eff}} \leq 7500 \text{ K}$.

Table 7 and Figure 10 reveal that methods G3, G6, G7, and G8 exhibit the highest offsets relative to the high-resolution analyses. The behavior of G3 (which comes from the neural network approach described in §4.6 above), is understood because that network was originally trained on a preliminary version of the SSPP, and hence it "inherited" whatever uncertainties existed in surface gravity estimates at that time. It is not presently clear what reasons, other than just the difficulty of extracting accurate estimates of $\log g$, might explain the large offsets of techniques G6, G7, and G8. Inspection of Figure 10 makes it clear that we could benefit from the inclusion of additional stars with lower surface gravities. Nevertheless, the adopted values for surface gravity by the SSPP are reasonably well distributed around the one-to-one correlation line. The offset and one-sigma scatter in the final adopted estimate of $\log g$ are +0.04 dex and 0.25 dex, respectively, which is surprisingly good for this difficult-to-estimate parameter.

It is clear from the comparison of the estimated metallicities from the SSPP in Table 8 and Figure 11 why we exclude the estimates M5 (the auto-correlation function method) and M6 (the Ca II triplet method) for the time being. The M5 estimates exhibit large (low) offsets for stars at higher metallicites, and a large overall scatter at lower metallicities (the latter is an expected behavior). The M6 estimates are systematically offset (high) from the expected correlation, and also have a larger scatter than desired. There is also a tendency for M3, the estimate obtained from the neural network method, to underestimate the metallicities of the more metal-rich stars. As mentioned previously, this is understood to be the result of training this technique on a previous version of the SSPP. We are in the process of re-calibrating all three estimators, and expect to implement them in future versions of the SSPP.

Inspection of Figure 11 indicates that we could benefit from the addition of more stars with intermediate metallicities, as well as for stars at the lowest metallicities. The mean offset (−0.04 dex) and one-sigma scatter (0.21 dex) of the residuals between the SSPP predictions of [Fe/H] and the high-resolution analysis are quite encouraging, at least over the parameter space explored to date.

It is obvious that there still exists a "clustering effect" in the low-metallicity regime ([Fe/H] ∼ -2.0) in Figure 11. This stems from analysis of HET and Keck-ESI data by T.S..

In the analysis of the HET and Keck-ESI spectra, the wavelength region of $4800 - 5300$ Å is used for deriving the parameters. This region includes the H$\beta$, Mg I$b$, Fe I , Fe II , Ca I, and Cr I lines. The H$\beta$ region is sensitive to $T_{\mathrm{eff}}$, irrespective of metallicity, and is independent of log $g$ for $T_{\mathrm{eff}}$ cooler than 6000 K; as a result $T_{\mathrm{eff}}$ estimates have less influence from [Fe/H] and log $g$. However, log $g$ and [Fe/H] have similar effects on Mg I and other neutral lines. At higher metallicities, the Mg I$b$ lines develop strong wings, and are sensitive to log $g$. Therefore, one can de-couple the variation in $\chi^2$ due to changes in log $g$ and [Fe/H] much better at higher metallicities. At low metallicities the wings are not visible, increasing the degeneracy between [Fe/H] and log $g$.

In summary, based on the sets of parameter comparisons with the high-resolution analysis, in the effective temperature range of 4500 K $\leq T_{\mathrm{eff}} \leq$ 7500 K the SSPP is capable of producing estimates of the atmospheric parameters for SDSS-I/SEGUE stars to precisions of $\sigma(T_{\mathrm{eff}})$, $\sigma(\log g)$, and $\sigma([\mathrm{Fe/H}])$ of 135 K, 0.25 dex, and 0.21 dex, respectively, after adding systematic offsets quadratically. These uncertainties will be slightly reduced if we take into account the error contribution from the high resolution analysis as in Paper III (e.g., in a manner of quadratic subtraction) . However, it should be kept in mind that the stars for which these comparisons are carried out are among the very brightest observed with SDSS, and the overall precision of parameter determination will decline for fainter stars. We are in the process of quantifying the accuracies and precisions of atmospheric parameter determinations as a function of $S/N$, and will report on these results in due course.

Paper III takes a slightly different approach to derive empirical external errors of the parameters determined by the SSPP. In this paper, final external uncertainties are $\sigma(T_{\mathrm{eff}}) =$ 130 K, $\sigma(\log g) = 0.21$ dex, and $\sigma([\mathrm{Fe/H}]) = 0.11$ dex.

## 8.2. Validation from Galactic Open and Globular Clusters

Galactic open and globular clusters provide nearly ideal testbeds for validation of the stellar atmospheric parameters estimated by the SSPP. In most clusters, it is expected that the member stars were born simultaneously out of well-mixed, uniform-abundance gas at the same location in the Galaxy. Therefore, the member stars should exhibit very similar elemental-abundance patterns. During the course of SDSS-I and tests for SEGUE, we have secured photometric and spectroscopic data for the clusters M 13, M 15, NGC 2420, and M 67, and can make use of these clusters for validation of the atmospheric parameters obtained by the SSPP. A more detailed description of this validation can be found in Paper II, to which we refer the interested reader. Here, we briefly report on just the results of the [Fe/H] comparisons as a function of $g - r$ color.

Figure 12 shows, from top to bottom, the SSPP estimated metallicities for likely member stars of M 15, M 13, NGC 2402, and M 67 as a function of $g - r$ color. The solid red line is the literature value of metallicity, reported by Harris (1996) for M 15 and M 13, and Gratton (2000) for NGC 2420 and M 67, while the dashed green line indicates the Gaussian mean SSPP [Fe/H] for the likely member stars (solid dots). Inspection of this Figure indicates that the SSPP obtains results for M 15 that are about 0.14 dex higher than the literature value, agrees quite well with the intermediate-metallicity clusters, and underestimates the metallicity of M 67 by about 0.3 dex. In addition, their appears to exist a slight trend of declining [Fe/H] with respect to $g - r$ in these determinations, at least for the more metal-rich clusters. Observations of additional clusters, especially of intermediate and near-solar metallicities, will clearly be helpful.

## 9. Assignment of Spectral Classifications for Early and Late-Type Stars

It is often useful to group stars into rough MK spectral classifications. It should be kept in mind, however, that for this, and any other exercise of assigning MK spectral types, that the MK system *does not apply* to stars other than Population I. That is, typing of metal-poor Population II stars is, *by definition*, not a strictly valid procedure. Nevertheless, the SSPP attempts to carry out this exercise using two approaches. The first is based on the spectral type listed in the ELODIE database for the best template match obtained for the determination of radial velocity (as described above), and applies to stars with spectral classes O to M.

For the coolest stars, measurement of accurate values of $T_{\rm eff}$, $\log g$, and [Fe/H] from spectra dominated by broad molecular features becomes extremely difficult (e.g., Woolf & Wallerstein 2006). As a result, the SSPP does not estimate atmospheric parameters for stars with $T_{\rm eff} < 4500$ K, but instead estimates the MK spectral type of each star using the "Hammer" spectral-typing software developed and described by Covey et al. (2007) [2]. The Hammer code measures 23 spectral indices, including atomic lines (H, Ca I, Ca II, Fe I, Mg I, Na I) and molecular bandheads (CN, G band, TiO, VO, CaH, FeH), as well as a select set of broadband color ratios. The best-fit spectral type of each target is assigned by comparison to the grid of indices measured from more than 1000 spectral-type standards derived from spectral libraries of comparable resolution and coverage (Allen & Strom 1995; Prugniel & Soubiran 2001; Hawley et al. 2002; Bagnulo et al. 2003; Le Borgne et al. 2003; Valdes et al.

---

[2]The Hammer has been made available for community use: the IDL code can be downloaded from http://www.cfa.harvard.edu/~kcovey/

2004; Sańchez-Blázquez et al. 2006).

Tests of the accuracy of the Hammer code with degraded ($S/N \sim$ 5/1) STELIB (Le Borgne et al. 2003), MILES (Sánchez-Blázquez et al. 2006), and SDSS (Hawley et al. 2002) dwarf template spectra reveal that the Hammer code assigns spectral types accurate to within $\pm$ 2 subtypes for K and M stars. The Hammer code also returns results for warmer stars, but as the set of indices used is optimized for cool stars, typical uncertainties are $\pm 4$ subtypes for A-G stars at $S/N \sim 5/1$; in this temperature regime, the SSPP atmospheric parameters are a more reliable indicator of $T_{\mathrm{eff}}$.

Given the science goals of, in particular, the SEGUE program, we emphasize two limitations to the accuracy of spectral types derived by the Hammer code:

- The Hammer code uses spectral indices derived from dwarf standards; spectral types assigned to giant stars will likely have larger, and systematic, uncertainties.

- The Hammer code was developed in the context of SDSS-I's high Galactic latitude spectroscopic program; the use of broadband color ratios in the indices will likely make the spectral types estimated by the Hammer code particularly sensitive to reddening. Spectral types derived in areas of high extinction (i.e., low-latitude SEGUE plates) should be considered highly uncertain until verified with reddening-insensitive spectral indices.

## 10. Preliminary Distance Estimates

A number of techniques are presently being explored by members of the SEGUE team in order to derive the best available estimates of distances for stars in the SDSS/SEGUE database. Many rely on the existence of either theoretical or empirical transformations of the substantial amount of photometric data that exists for Galactic clusters obtained with photometric systems other than $ugriz$. These will be reported on in due course (Morrison et al. 2007, in preparation). For now, the SSPP assigns preliminary distance estimates for stars of different luminosity classifications based on the empirical fits of Beers et al. (2000) to the observed color-magnitude diagrams of Galactic clusters of different metallicities and with reasonably well-known distances (in the Johnson $V$, $B - V$ system). For convenience, we use the same transformations as mentioned above, based on the work of Zhao & Newberg (2006); $V = g - 0.561(g - r) - 0.004$, and $B - V = 0.187 + 0.916(g - r)$.

Beers et al. (2000) argue that their distances should be accurate to on the order of $10 - 20\%$; a typical value of 15% can be adopted for our distance estimates, although this needs

to be confirmed with future work.

The SSPP does *not* make a stellar luminosity classification, but rather, it provides the atmospheric parameters from which the user can make an appropriate choice. Distance estimates are obtained for the following rough luminosity classes: Dwarf, Main-Sequence Turnoff, Giant, Asymptotic Giant Branch, and Field Horizontal-Branch. Note that distance estimates are obtained for all (feasible) cases where a star may fall into one or more of these classifications, but only one of the listed distances is likely to apply to a given star. The choice is up to the user.

Two other methods for distance estimates are obtained by the SSPP. The first is described by Allende Prieto et al. (2006), to which the interested reader is referred for a detailed description. The second is based on the isochrones in the *ugriz* system developed by Girardi et al. (2004). Our initial tests of this method did not converge as well as was hoped. Although we will continue to work on this, and other methods, for distance estimates, we do not fully implement the Girardi et al. isochrone approach in the SSPP for the DR6 (Adelman-McCarthy et al. 2007b) release.

## 11. Conclusions

We have described the development and execution of the SEGUE Stellar Parameter Pipeline (SSPP), which makes use of multiple approaches in order to estimate the fundamental stellar atmospheric parameters (effective temperature, $T_{eff}$, surface gravity, log $g$, and metallicity, parameterized by [Fe/H]) for stars with spectra and photometry obtained during the course of the original Sloan Digital Sky Survey (SDSS-I) and its current extension (SDSS-II/SEGUE).

The use of multiple approaches allows for an empirical determination of the internal errors for each derived parameter, based on the range of the reported values from each method. From consideration of about 140,000 spectra of stars obtained during SDSS-I and SEGUE that have derived stellar parameters available in the range 4500 K $\leq T_{eff} \leq$ 7500 K, typical internal errors obtained by the SSPP are $\sigma(T_{eff}) = 73$ K (s.e.m), $\sigma(\log g) = 0.19$ (s.e.m), and $\sigma([Fe/H]) = 0.10$ (s.e.m). Paper III points out that the internal scatter estimates obtained from averaging the multiple estimates of the parameters produced by the SSPP underestimate the external errors, owing to the fact that several methods in the SSPP use similar same parameter indicators and atmospheric models.

The results of a comparison with an average of two different high-resolution spectroscopic analyses of 124 SDSS-I/SEGUE stars suggests that the SSPP is able to determine $T_{eff}$,

log $g$, and [Fe/H] to precisions of 135 K, 0.26 dex, and 0.21 dex, respectively, after combining small systematic offsets quadratically for stars with 4500 K $\leq T_{\rm eff} \leq$ 7500 K. These errors differ slightly from the those obtained by Paper III ($\sigma(T_{\rm eff})$ = 130 K, $\sigma(\log g)$ = 0.21 dex, and $\sigma([{\rm Fe/H}])$ = 0.11 dex), even though they share a common set of high-resolution calibration observations. This arises because Paper III derived the external uncertainties of the SSPP only taking into account the stars observed with the HET (on the grounds of internal consistency). The sample referred to as OTHERS in Paper III exhibits somewhat larger scatter in its parameters, when compared with those determined by the SSPP. Observation of several hundred additional stars from SDSS-I/SEGUE with HET is now underway. Thus, in the future, we will be able to use a homogeneous sample gathered by HET in our tests. Also, additional high-resolution data for stars outside of our adopted temperature range will enable tests for both cooler and warmer stars.

Considering the internal scatter from the multiple approaches and the external uncertainty from the comparisons with the high-resolution analysis together, the typical uncertainty in the stellar parameters delivered by the SSPP are $\sigma(T_{\rm eff})$ = 154 K, $\sigma(\log g)$ = 0.31 dex, and $\sigma([{\rm Fe/H}])$ = 0.23 dex, over the temperature range 4500 K $\leq T_{\rm eff} \leq$ 7500 K.

However, it should be kept in mind that the errors stated above apply for the very highest $S/N$ spectra obtained from SDSS ($S/N > 50/1$), as only quite bright stars were targeted for high-resolution observations. In addition, outside of the quoted temperature range (4500 K $\leq T_{\rm eff} \leq$ 7500 K), we presently do not have sufficient high-resolution spectra to fully test the parameters obtained by the SSPP.

The results of a comparison with likely member stars of a sample of Galactic open and globular clusters suggest that SSPP may slightly overestimate [Fe/H] (by $\sim$ 0.15 dex) for stars with [Fe/H] $< -2.0$, and underestimate [Fe/H] (by $\sim$ 0.30 dex) for stars with near-solar metallicities. Slight trends of [Fe/H] with $g - r$ are noticed for the higher metallicity clusters as well, although further data will be needed in order to verify this.

Approximate spectral types are assigned for stars, based on two methods, with differing limitations. A preliminary set of distance determinations for each star is also obtained, although future work will be required in order to identify the optimal method.

We conclude that the SSPP determines sufficiently accurate and precise radial velocities and atmospheric parameter estimates, at least for stars in the effective temperature range from 4500 K to 7500 K, to enable detailed explorations of the chemical compositions and kinematics of the thick-disk and halo populations of the Galaxy.

## REFERENCES

Abazajian, K., et al. 2005, AJ, 129, 1755

Abazajian, K., et al. 2004, AJ, 128, 502

Abazajian, K., et al. 2003, AJ, 126, 2081

Adelman-McCarthy, J. K., et al. 2007a, ApJS, 172, 634

Adelman-McCarthy, J. K., et al. 2007b, ApJS, accepted

Adelman-McCarthy, J. K., et al. 2006, ApJS, 162, 38

Allen, L. E., & Strom, K. M. 1995, AJ, 109, 1379

Allende Prieto, C., Beers, T. C., Wilhelm, R., et al. 2006, ApJ, 636, 804

Allende Prieto, C., et al. 2007, AJ, submitted (Paper III)

Alvares, R. & Plez, B. 1998, A&A, 330, 1109

Asplund, M., Grevesse, N., & Sauval, A. J. 2005, EAS Publications Series, 17, 21

Bagnulo, S., et al. 2003, The Messenger, 114, 10

Barklem, P. S. & O'Mara, B. J. 1998, MNRAS, 300, 863

Beers, T. C., Flynn, K., & Gebhardt, C. 1990, AJ, 100, 32

Beers, T. C., Rossi, S., Norris, J. E., Ryan, S. G.,& Shefler, T. 1999, ApJ, 506, 892

Beers, T. C., Preston, G. W., & Shectman, S. A. 1992, AJ, 103, 1987

Beers, T. C., Preston, G. W., & Shectman, S. A. 1985, AJ, 90, 2089

Beers, T. C., et al. 2000, AJ, 119, 2866

Castelli, F. & Kurucz, R. L. 2003, IAU Symposium, 210, A20

Castelli, F., Gratton, R. G., & Kurucz, R. L. 1997, A&A, 318, 841

Cayrel, R. 1988, IAUS, 132, 345C

Cayrel de Strobel, G., Soubiran, C., & Ralite, N. 2001, A&A, 373, 159

Cenarro A.J., Cardiel N., Gorgas J., Peletier R.F., Vazdekis A., & Prada F. 2001a, MNRAS, 326, 959

Cenarro A. J., Gorgas J., Cardiel N., Pedraz S., Peletier R.F., & Vazdekis, A. 2001b, MNRAS, 326, 981

Christlieb, N. 2003, Rev. Mod. Astron., 16, 191

Covey, K. R., et al. 2007, AJ, in press

Fukugita, M., Ichikawa, T., Gunn, J.E., Doi, M., Shimasaku, K., & Schneider, D.P. 1996, AJ, 111, 1748

Girardi, L., Grebel, E. K., Odenkirchen, M., & Chiosi, C. 2004, A&A, 422, 205

Gratton, R. 2000, ASP Conf. Ser. 198, 225

Gray, R. O. & Corbally, C. J. 1994, AJ, 107, 742

Grevesse, N. & Sauval, A. J. 1998, SSRv, 85, 161G

Gunn, J. E., et al. 2006, AJ, 131, 2332

Gunn, J. E., et al. 1998, AJ, 116, 3040

Harris, W. E. 1996, AJ, 112, 1487

Hawley, S. L., et al. 2002, AJ, 123, 3409

Ivezić, Z., et al. 2007, ApJ, submitted

Koesterke, L., Allende Prieto, C., & Lambert, D. L. 2007, ApJ, submitted

Kupka, F., Piskunov, N., Ryabchikova, T. A., Stemples, H. C., & Weiss, W. W. 1999, A&AS, 138, 119

Kurucz, R. L. 1993, private communication

Kurucz, R. L. 1993, Kurucz CD-ROM 13, ATLAS9 Stellar Atmosphere Programs and 2 km/s grid (Camgridge: SAO)

Le Borgne, J.-F., et al. 2003, A&A, 402, 433

Lee, Y. S., Beers, T. C., Sivirani, T., et al. 2007b, AJ, submitted (Paper II)

Lupton, R., et al. 2001, in ASP Conf. Ser. 238, Astronomical Data Analysis Software and Systems X, ed. F. R. Harnden, Jr., F. A. Primini, and H. E. Payne (San Francisco: Astr. Soc. Pac.), p. 269

Morrison, H. L., et al. 2007, in preparation

Morrison, H. L., Norris, J., Mateo, M., et al. 2003, AJ, 125, 2502

Moultaka, J., Ilovaisky, S. A., Prugniel, P., & Soubiran, C. 2004, PASP, 116, 693

Nelder, J. & Mead, R. 1965, Comput. J., 7, 308

Pier, J.R., et al. 2003, AJ, 125, 1559

Plez, B. & Cohen, J. G. 2005, A&A, 434, 1117

Prugniel, Ph. & Soubiran, C., 2001, A&A, 369,1048

Re Fiorentin, P., Bailer-Jones, C. A. L., Lee, Y. S. et al. 2007, A&A, 467, 1373

Reimers, D. & Wisotzki, L. 1997, Msngr, 88, 14

Sánchez-Blázquez, P., Peletier, R. F, Jiménez-Vicente, J., et al. 2006, MNRAS, 371, 703

Schlegel, D. J., Finkbeiner, D. P., & Davis, M. 1998, ApJ, 500, 525

Stoughton, C., et al. 2002, AJ, 123, 485

Strauss, M & Gunn, J. E. 2001, SDSS Data Release 3, Technical Note (Baltimore: STScI), http://www.wdss.org/dr3/instruments/imager/index.html

Valdes, F., Gupta, R., Rose, J. A., Singh, H. P., & Bell, D. J. 2004, ApJS, 152, 251

Wisotzki, L., Christlieb, N., Bade, N., et al. 2000, A&A, 358, 77

Wilhelm, R., Beers, T., & Gray, R. 1999, AJ, 117, 2308 (WBG99)

Woolf, V. M. & Wallerstein, G. W. 2006, PASP, 118, 218

York, D. G., et al. 2000, AJ, 120, 1579

Zhao, C. & Newberg, H. J. 2006, astro-ph/0612034
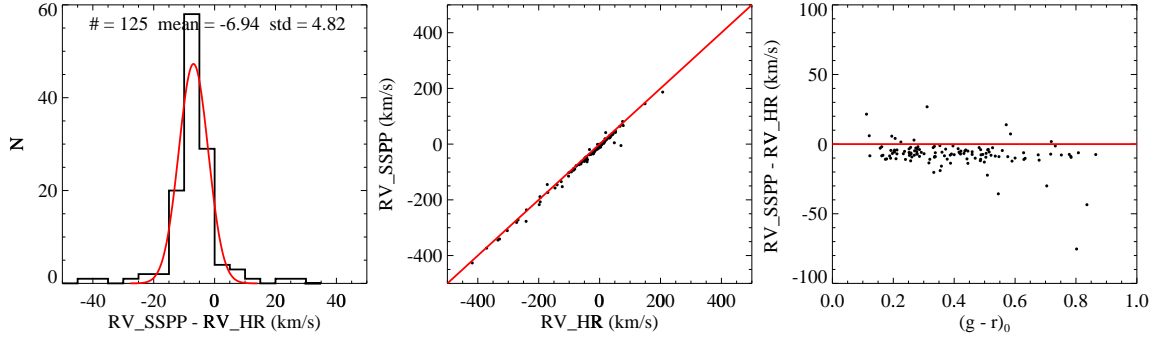
Fig. 1.— A comparison plot of the radial velocity adopted by the SSPP with that measured by the high-resolution analyses. There were three different measurements for stars observed with HET for the high-resolution data. A simple average of the three measurement was taken for this comparison. An offset of $-6.9$ km s$^{-1}$ is noticed from the Gaussian fit to the residuals. This offset appears constant with $g - r$ in the right-hand panel.
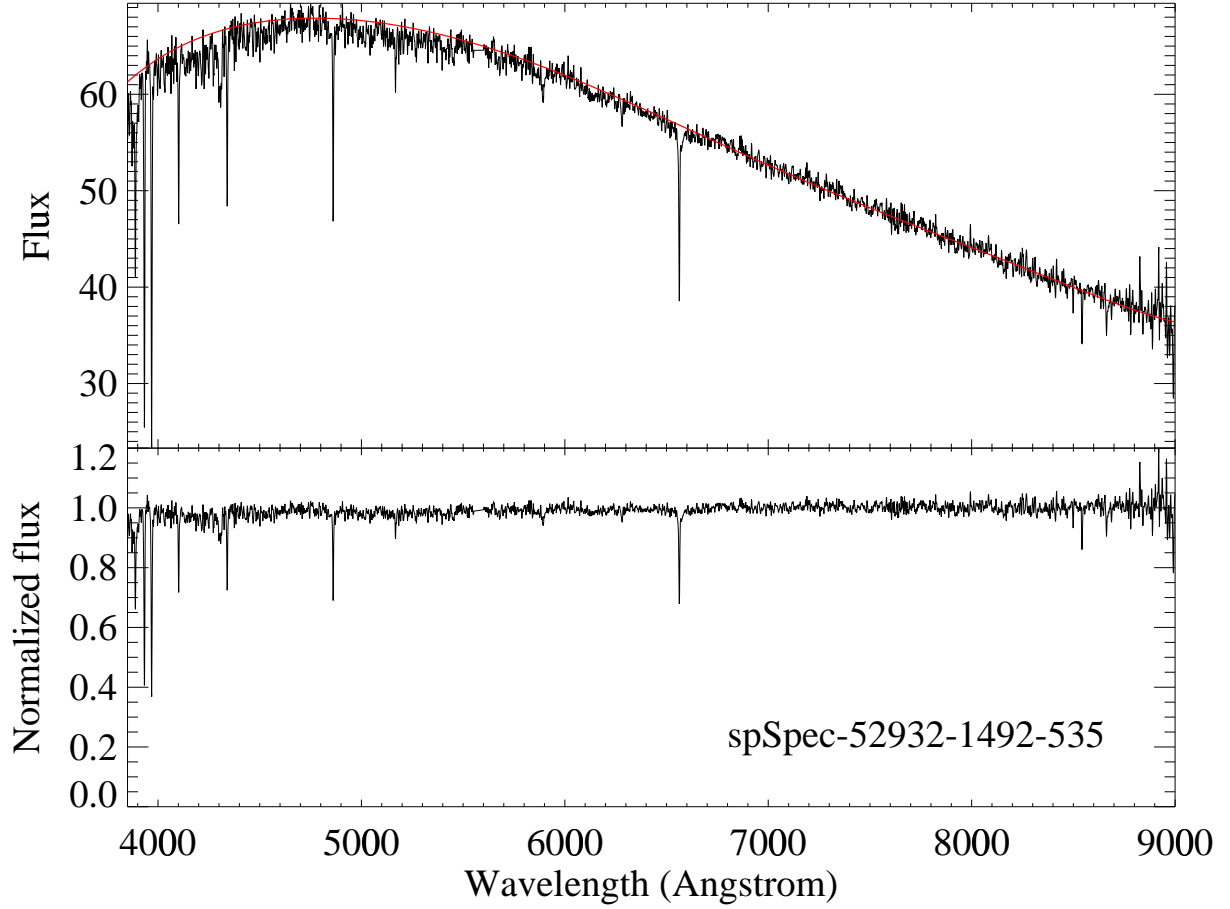
Fig. 2.— An example of a fitted global continuum. The red line in the upper panel is the fitted continuum over the 3850−9000 Å wavelength range; the black line is the observed spectrum. The bottom panel shows the normalized flux.
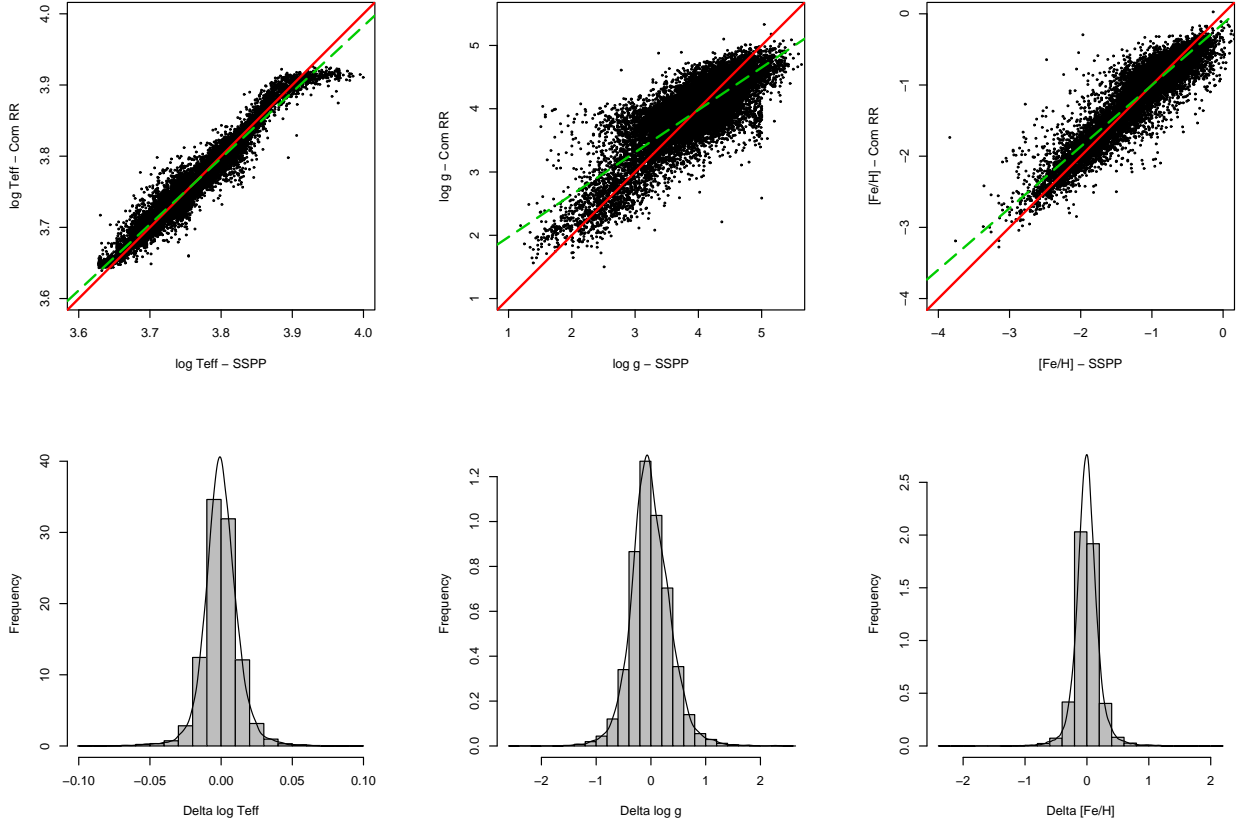
Fig. 3.— Atmospheric parameter estimation with the RR model. We compare our estimated $\log T_{\mathrm{eff}}$, $\log g$, and [Fe/H] with those from a preliminary version of the SSPP on the 19,000 stars in the evaluation set. The perfect correlation and a linear fit to the data are shown with the solid and dashed lines respectively. The histogram of the discrepancies (our estimates minus SSPP estimates) are shown in the lower panels.
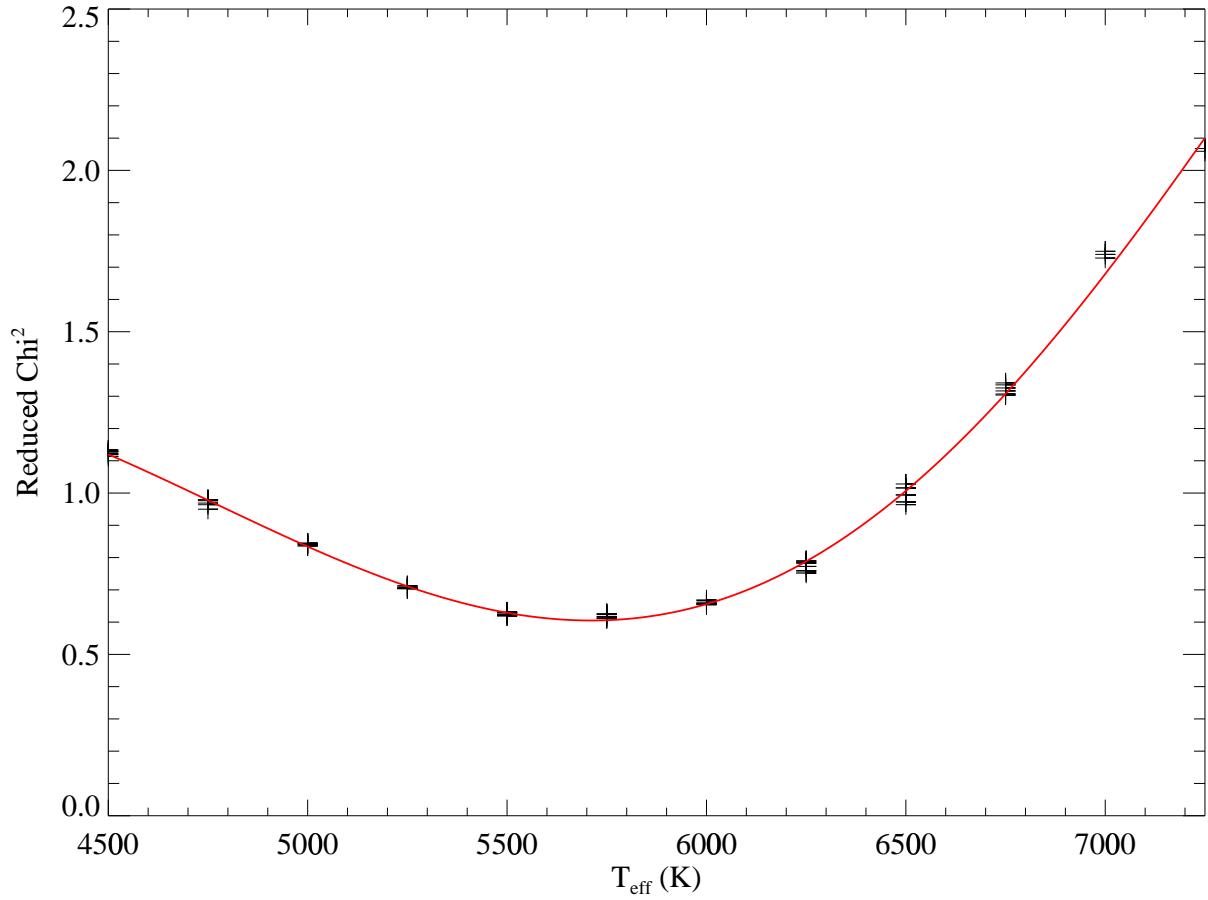
Fig. 4.— An example of finding a minimum reduced $\chi^2$ value as a function of $T_{\rm eff}$. The crosses are the remaining values after application of an iterative rejection scheme. The red curve is the final fitted function.
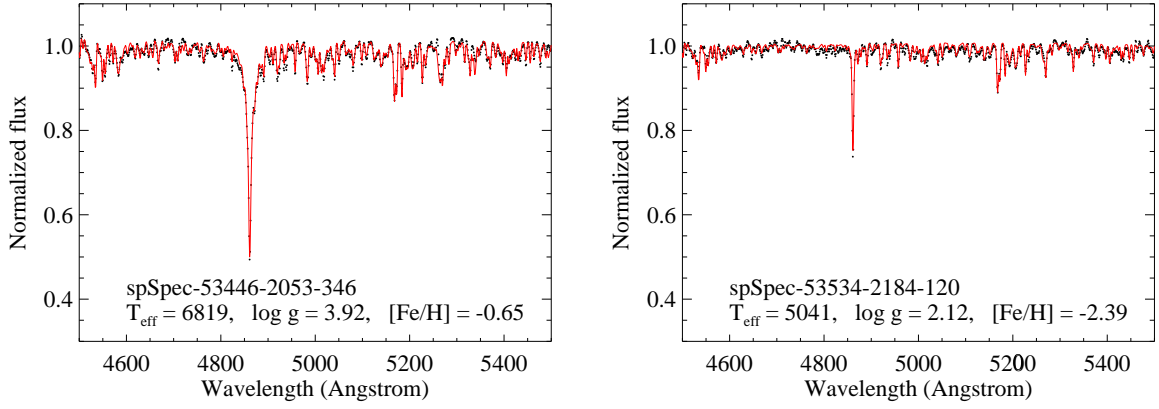
Fig. 5.— Two examples of the results of the application of the NGS1 grid, for a warmer, metal-rich star (left panel), and for a cooler, metal-poor star (right panel). The black dots are the observed data points; the red lines are synthetic spectra generated with the atmospheric parameters adopted by the technique.
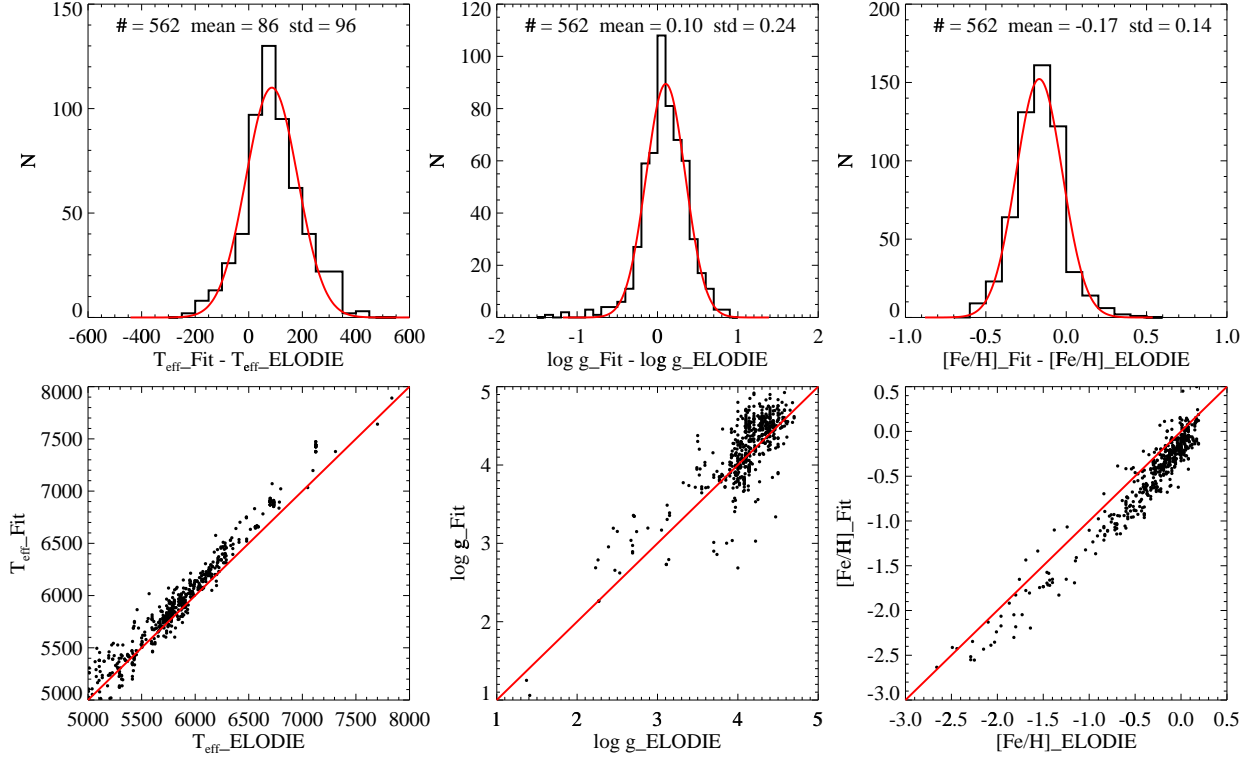
Fig. 6.— Comparison of parameters obtained from the `NGS1` grid (FIT) with those from the ELODIE spectral library (ELODIE). It appears that the temperature and gravity are over-estimated by 86 K and 0.10 dex, respectively, and the metallicity is under-estimated by 0.17 dex, based on Gaussian fits to the residuals.
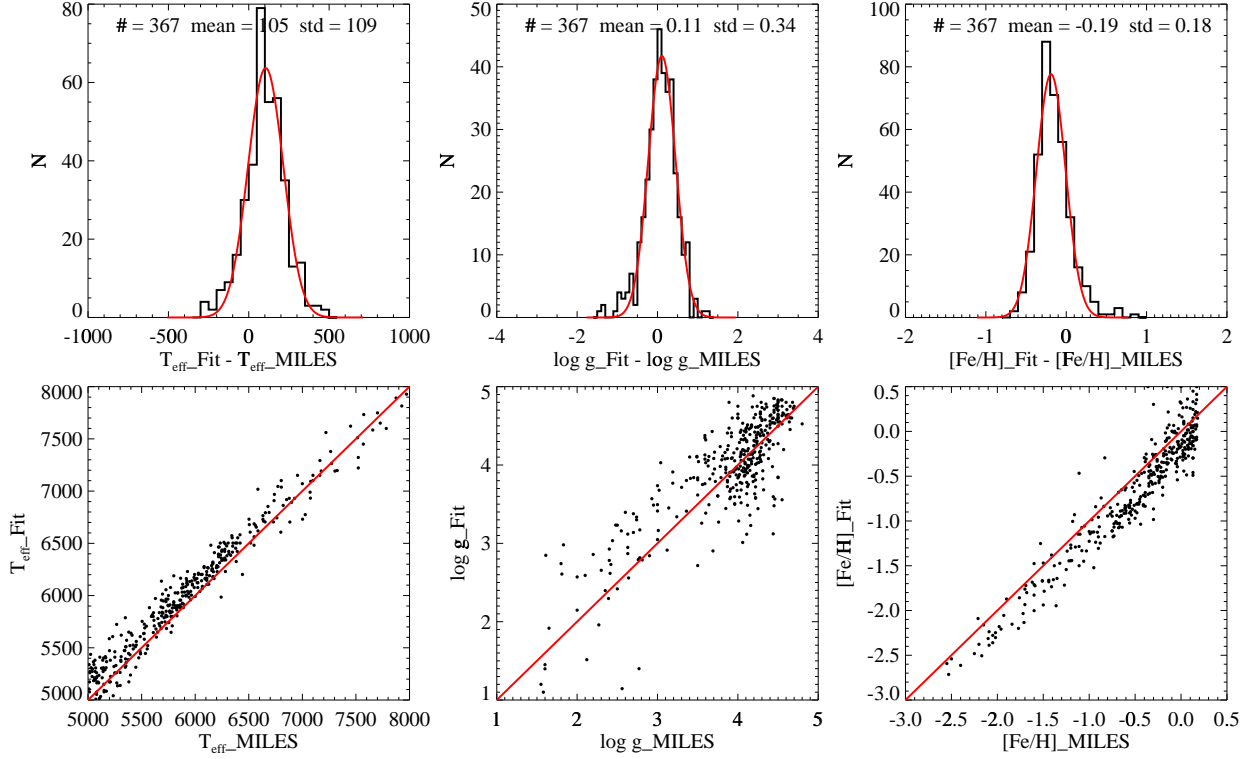
Fig. 7.— Comparison of parameters obtained from the `NGS1` grid (FIT) with those from the MILES spectral library (MILES). It appears that the temperature and gravity are over-estimated by 105 K and 0.11 dex, respectively, and the metallicity is under-estimated by 0.19 dex, based on Gaussian fits to the residuals.
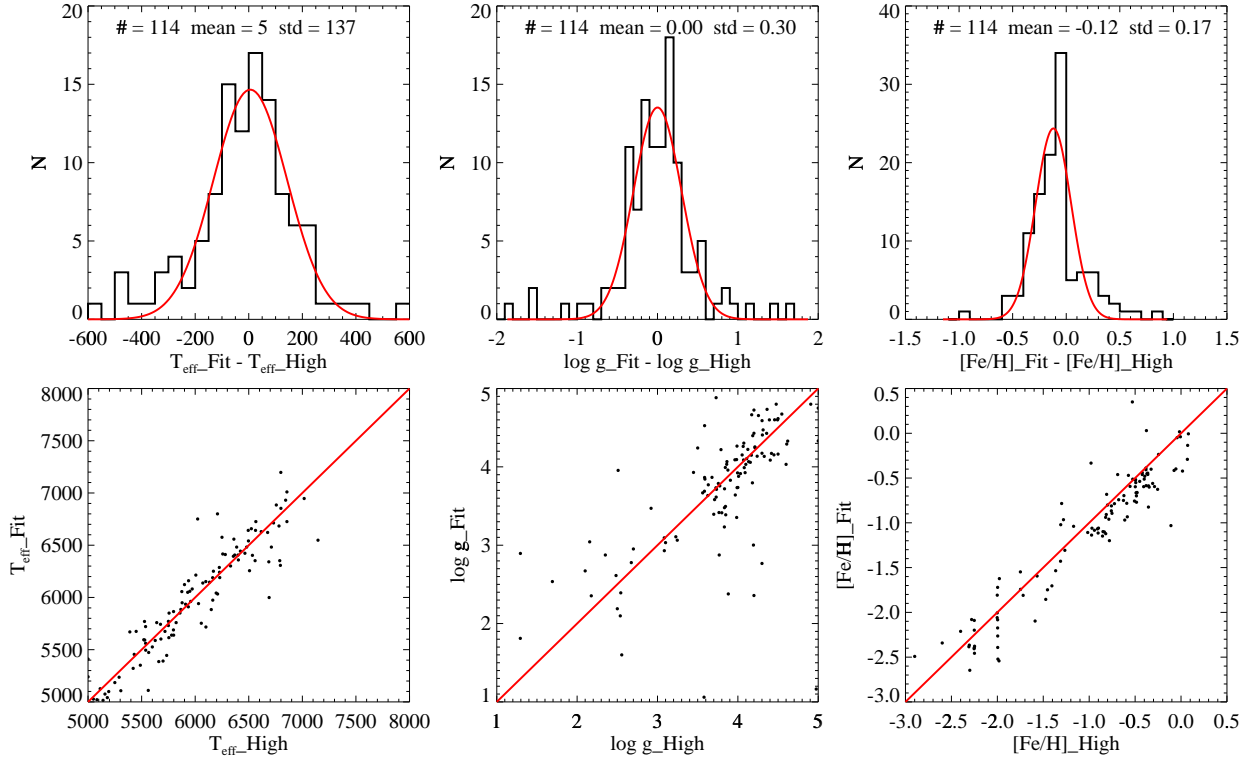
Fig. 8.— Comparison of parameters obtained from the `NGS1` grid (FIT) with those from the analysis of high-resolution spectroscopy of SDSS-I/SEGUE stars (High). The parameters from the high-resolution data are averages of two independent analyses. Unlike the results from comparisons with the ELODIE and MILES spectral libraries, the effective temperature and the surface gravity present almost no offsets.
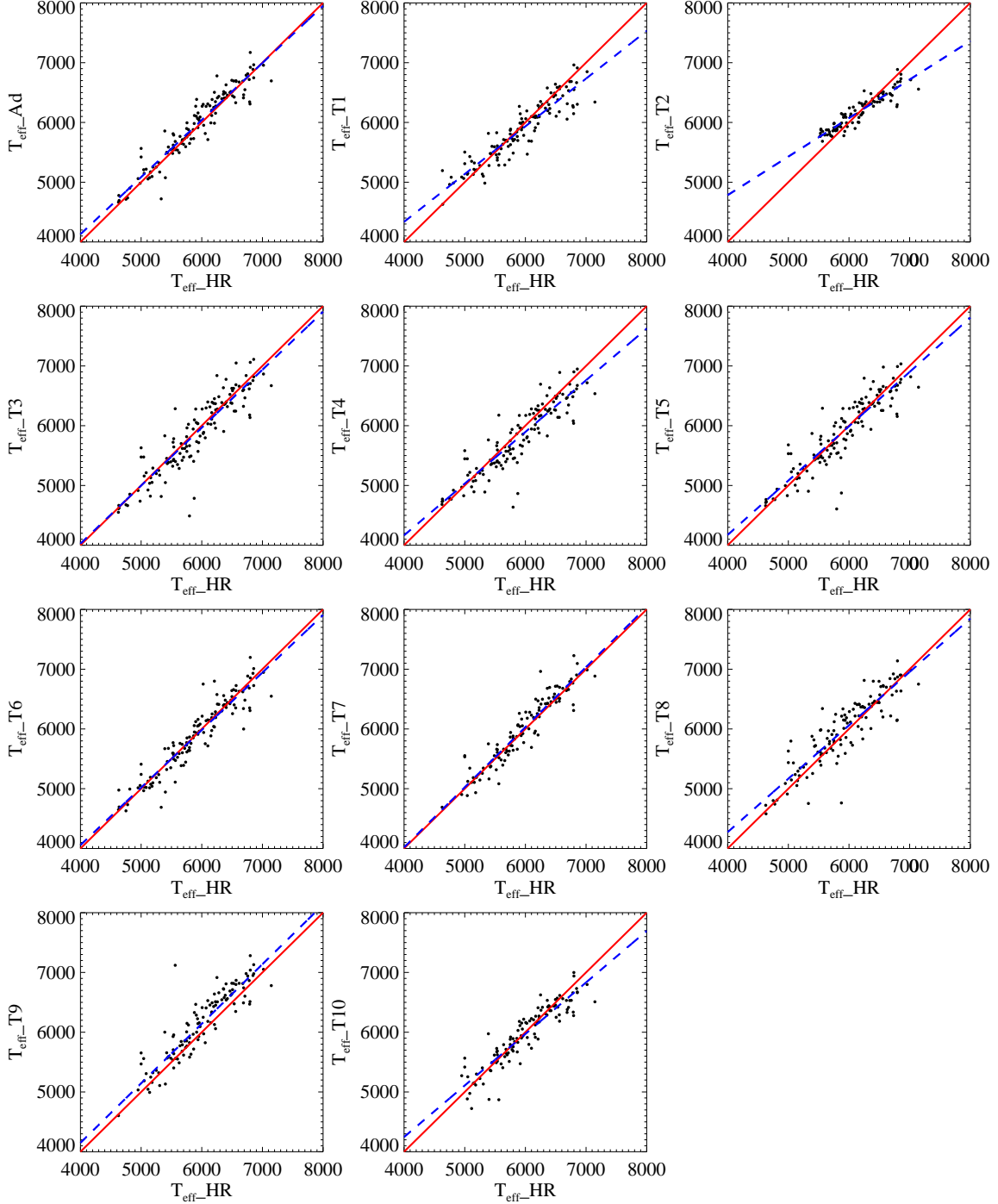
Fig. 9.— Comparison of effective temperatures estimated from individual methods with those from the analysis of high-resolution spectra of SDSS-I/SEGUE stars. 'HR' indicates the high-resolution analysis results. The red solid line is the one-to-one correlation line; the blue dashed line is the least squares fit to the data.
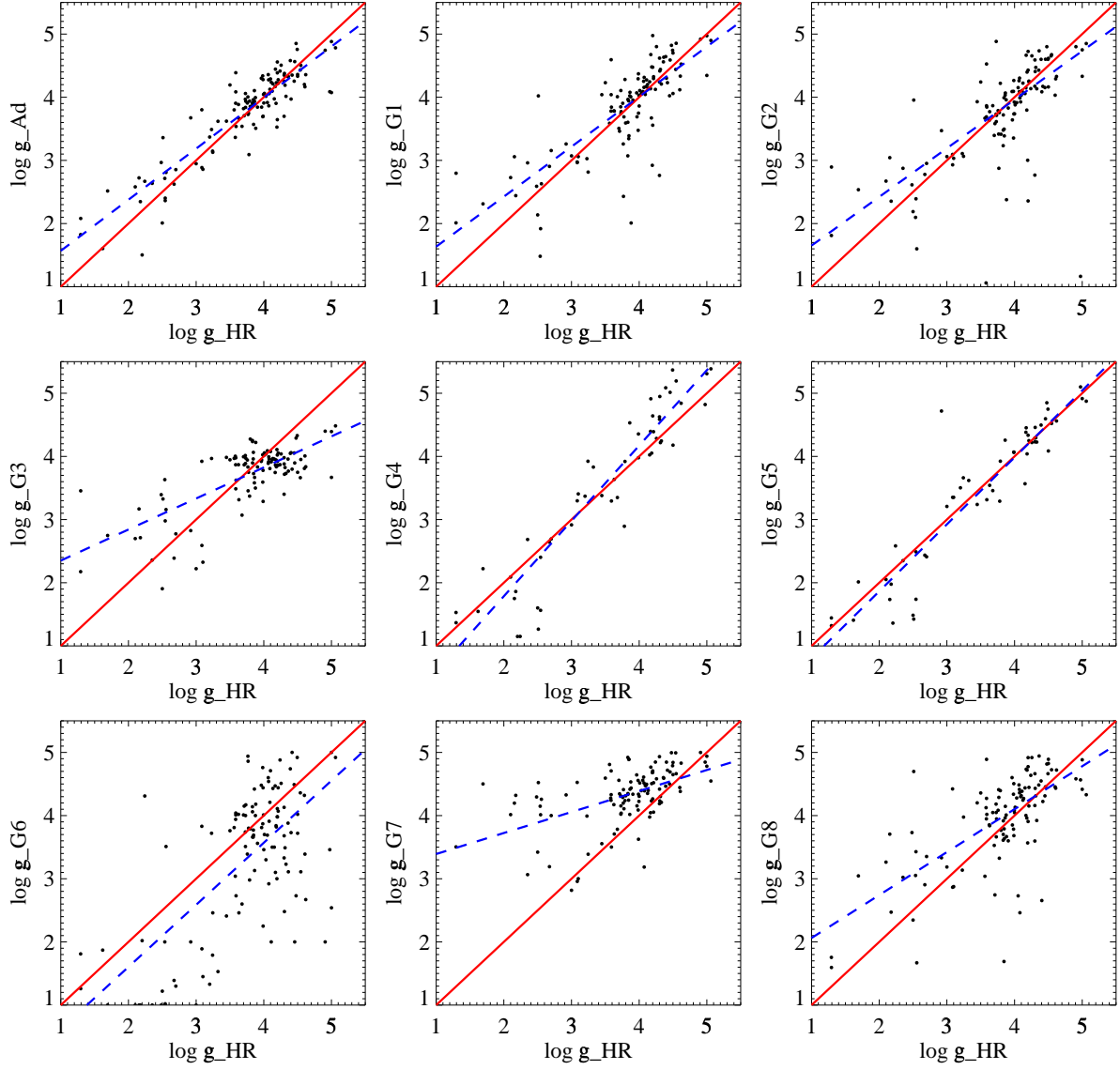
Fig. 10.— Same as Fig. 9, but for surface gravities.
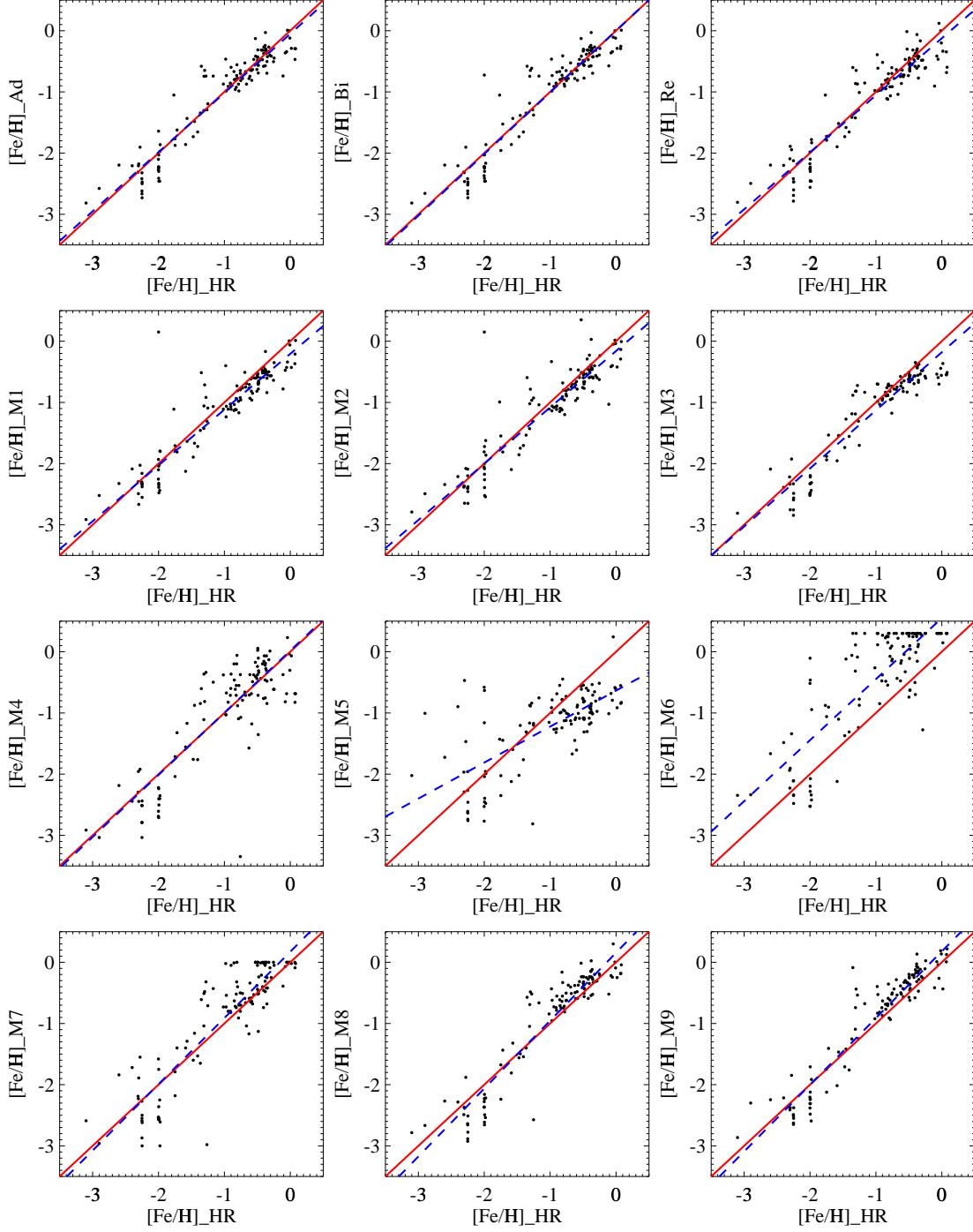
Fig. 11.— Same as Fig. 9, but for metallicities.
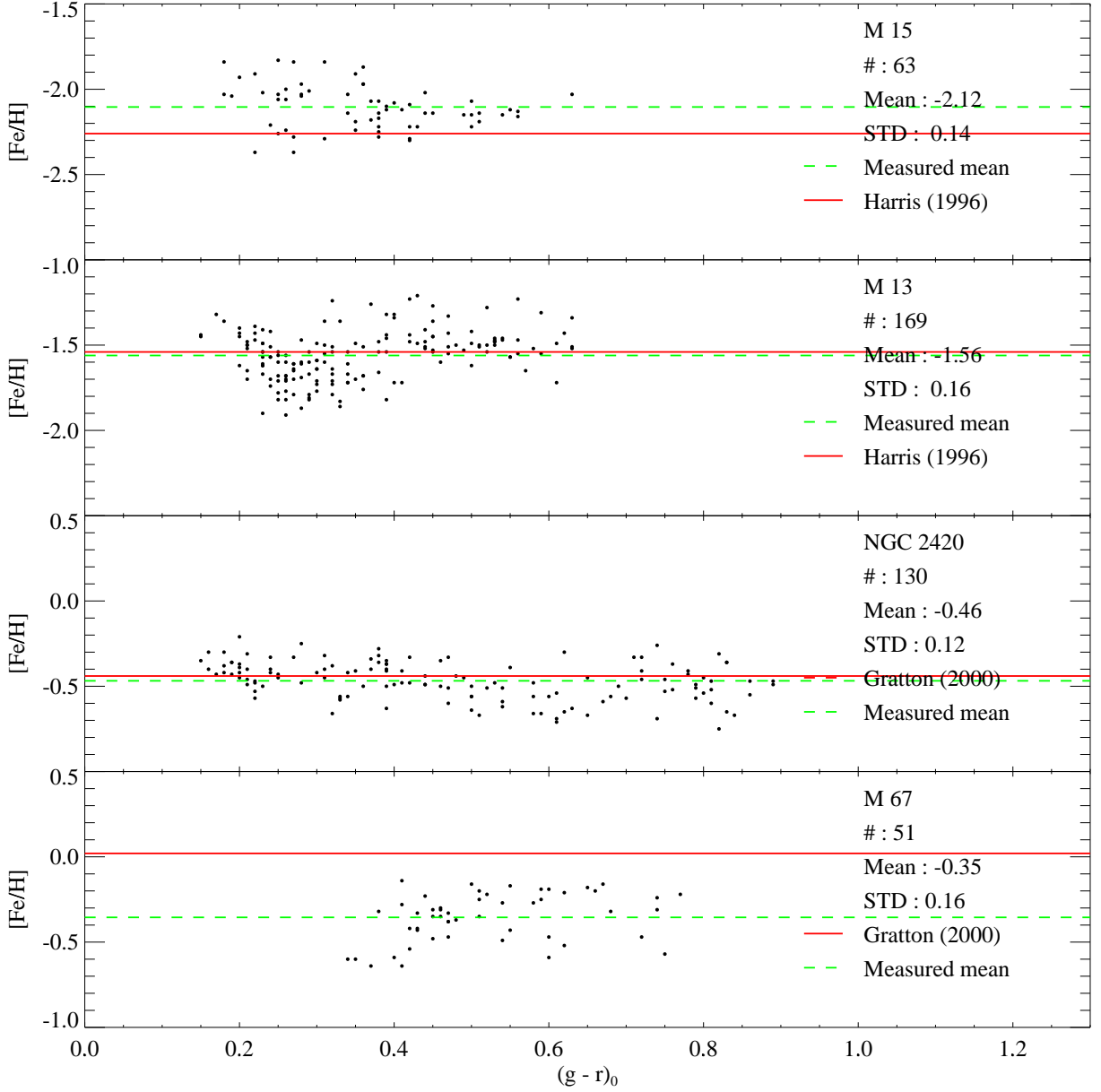
Fig. 12.— SSPP estimated metallicities with respect to $g - r$ for member stars of M 15, M 13, NGC 2420, and M 67. The green dashed line is the Gaussian average of the likely member stars of each cluster. See Paper II for a more detailed discussion of the selection of member stars and calculation of the Gaussian means. The red line is the adopted literature value. M 15 and M 13 are taken from Harris (1996); NGC 2420 and M 67 are taken from Gratton (2000).

Table 1.   Summary of High-Resolution Spectroscopy for SDSS and SEGUE Stars

| Telescope | Instrument | Resolving power | Wavelength coverage (Å) | Number of stars |
|-----------|-----------|-----------------|-------------------------|-----------------|
| Keck - I | HIRES | 45000 | 3800−10000 | 11 |
| Keck - II | ESI | 6000 | 3800−10000 | 25 |
| HET | HRS | 15000 | 4400−8000 | 110 |
| Subaru | HDS | 45000 | 3000−8000 | 9 |

Table 2.   Line Band and Sideband Widths and Format of the Output from the SSPP

| Column | Format | Description | Central (Å) | Width (Å) | Red (Å) | Width (Å) | Blue (Å) | Width (Å) |
|---|---|---|---|---|---|---|---|---|
| 1 | A22 | spSpec name | . . . | . . . | . . . | . . . | . . . | . . . |
| 2 | F8.3 | H8 (3) | 3889.0 | 3.0 | 3912.0 | 8.0 | 3866.0 | 8.0 |
| 3 | F8.3 | H8 (12) | 3889.1 | 12.0 | 4010.0 | 20.0 | 3862.0 | 20.0 |
| 4 | F8.3 | H8 (24) | 3889.1 | 24.0 | 4010.0 | 20.0 | 3862.0 | 20.0 |
| 5 | F8.3 | H8 (48) | 3889.1 | 48.0 | 4010.0 | 20.0 | 3862.0 | 20.0 |
| 6 | F8.3 | Ca II K12 (12) | 3933.7 | 12.0 | 4010.0 | 20.0 | 3913.0 | 20.0 |
| 7 | F8.3 | Ca II K18 (18) | 3933.7 | 18.0 | 4010.0 | 20.0 | 3913.0 | 20.0 |
| 8 | F8.3 | Ca II K6 (6) | 3933.7 | 6.0 | 4010.0 | 20.0 | 3913.0 | 20.0 |
| 9 | F8.3 | Ca II K | 3933.6 | 30.0 | 4010.0 | 5.0 | 3910.0 | 5.0 |
| 10 | F8.3 | Ca II HK+ | 3962.0 | 75.0 | 4010.0 | 5.0 | 3910.0 | 5.0 |
| 11 | F8.3 | H$\epsilon$ | 3970.0 | 50.0 | 4010.0 | 5.0 | 3910.0 | 5.0 |
| 12 | F8.3 | Ca II K16 (16) | 3933.7 | 16.0 | 4018.0 | 20.0 | 3913.0 | 10.0 |
| 13 | F8.3 | Sr II | 4077.0 | 8.0 | 4090.0 | 6.0 | 4070.0 | 4.0 |
| 14 | F8.3 | He I | 4026.2 | 12.0 | 4154.0 | 20.0 | 4010.0 | 20.0 |
| 15 | F8.3 | H$\delta$ (12) | 4101.8 | 12.0 | 4154.0 | 20.0 | 4010.0 | 20.0 |
| 16 | F8.3 | H$\delta$ (24) | 4101.8 | 24.0 | 4154.0 | 20.0 | 4010.0 | 20.0 |
| 17 | F8.3 | H$\delta$ (48) | 4101.8 | 48.0 | 4154.0 | 20.0 | 4010.0 | 20.0 |
| 18 | F8.3 | H$\delta$ | 4102.0 | 64.0 | 4154.0 | 20.0 | 4010.0 | 20.0 |
| 19 | F8.3 | Ca I | 4226.0 | 4.0 | 4232.0 | 4.0 | 4211.0 | 6.0 |
| 20 | F8.3 | Ca I (12) | 4226.7 | 12.0 | 4257.0 | 20.0 | 4154.0 | 20.0 |
| 21 | F8.3 | Ca I (24) | 4226.7 | 24.0 | 4257.0 | 20.0 | 4154.0 | 20.0 |
| 22 | F8.3 | Ca I (6) | 4226.7 | 6.0 | 4257.0 | 20.0 | 4154.0 | 20.0 |
| 23 | F8.3 | CH G-band | 4305.0 | 15.0 | 4367.0 | 10.0 | 4257.0 | 20.0 |
| 24 | F8.3 | H$\gamma$ (12) | 4340.5 | 12.0 | 4425.0 | 20.0 | 4257.0 | 20.0 |
| 25 | F8.3 | H$\gamma$ (24) | 4340.5 | 24.0 | 4425.0 | 20.0 | 4257.0 | 20.0 |
| 26 | F8.3 | H$\gamma$ (48) | 4340.5 | 48.0 | 4425.0 | 20.0 | 4257.0 | 20.0 |
| 27 | F8.3 | H$\gamma$ | 4340.5 | 54.0 | 4425.0 | 20.0 | 4257.0 | 20.0 |
| 28 | F8.3 | He I | 4471.7 | 12.0 | 4500.0 | 20.0 | 4425.0 | 20.0 |
| 29 | F8.3 | G-blue | 4305.0 | 26.0 | 4507.0 | 14.0 | 4090.0 | 12.0 |
| 30 | F8.3 | G-whole | 4321.0 | 28.0 | 4507.0 | 14.0 | 4096.0 | 12.0 |

Table 2—Continued

| Column | Format | Description | Central (Å) | Width (Å) | Red (Å) | Width (Å) | Blue (Å) | Width (Å) |
|---|---|---|---|---|---|---|---|---|
| 31 | F8.3 | Ba II | 4554.0 | 6.0 | 4560.0 | 4.0 | 4538.0 | 4.0 |
| 32 | F8.3 | $C_{12}C_{13}$ | 4737.0 | 36.0 | 4770.0 | 20.0 | 4423.0 | 10.0 |
| 33 | F8.3 | CC12 | 4618.0 | 256.0 | 4780.0 | 5.0 | 4460.0 | 10.0 |
| 34 | F8.3 | Metal-1 | 4584.0 | 442.0 | 4805.8 | 5.0 | 4363.0 | 5.0 |
| 35 | F8.3 | $H\beta$ (12) | 4862.3 | 12.0 | 4905.0 | 20.0 | 4790.0 | 20.0 |
| 36 | F8.3 | $H\beta$ (24) | 4862.3 | 24.0 | 4905.0 | 20.0 | 4790.0 | 20.0 |
| 37 | F8.3 | $H\beta$ (48) | 4862.3 | 48.0 | 4905.0 | 20.0 | 4790.0 | 20.0 |
| 38 | F8.3 | $H\beta$ | 4862.3 | 60.0 | 4905.0 | 20.0 | 4790.0 | 20.0 |
| 39 | F8.3 | $C_2$ | 5052.0 | 204.0 | 5230.0 | 20.0 | 4935.0 | 10.0 |
| 40 | F8.3 | $C_2$+Mg I | 5069.0 | 238.0 | 5230.0 | 20.0 | 4935.0 | 10.0 |
| 41 | F8.3 | MgH+Mg I+$C_2$ | 5085.0 | 270.0 | 5230.0 | 20.0 | 4935.0 | 10.0 |
| 42 | F8.3 | MgH+Mg I | 5198.0 | 44.0 | 5230.0 | 20.0 | 4935.0 | 10.0 |
| 43 | F8.3 | MgH | 5210.0 | 20.0 | 5230.0 | 20.0 | 4935.0 | 10.0 |
| 44 | F8.3 | Cr I | 5206.0 | 12.0 | 5239.0 | 8.0 | 5197.5 | 5.0 |
| 45 | F8.3 | Mg I+Fe II | 5175.0 | 20.0 | 5240.0 | 10.0 | 4915.0 | 10.0 |
| 46 | F8.3 | Mg I | 5183.0 | 2.0 | 5240.0 | 10.0 | 4915.0 | 10.0 |
| 47 | F8.3 | Mg I | 5170.5 | 12.0 | 5285.0 | 20.0 | 5110.0 | 20.0 |
| 48 | F8.3 | Mg I | 5176.5 | 24.0 | 5285.0 | 20.0 | 5110.0 | 20.0 |
| 49 | F8.3 | Mg I | 5183.5 | 12.0 | 5285.0 | 20.0 | 5110.0 | 20.0 |
| 50 | F8.3 | Na I | 5890.0 | 20.0 | 5918.0 | 6.0 | 5865.0 | 10.0 |
| 51 | F8.3 | Na (12) | 5892.9 | 12.0 | 5970.0 | 20.0 | 5852.0 | 20.0 |
| 52 | F8.3 | Na (24) | 5892.9 | 24.0 | 5970.0 | 20.0 | 5852.0 | 20.0 |
| 53 | F8.3 | $H\alpha$ (12) | 6562.8 | 12.0 | 6725.0 | 50.0 | 6425.0 | 50.0 |
| 54 | F8.3 | $H\alpha$ (24) | 6562.8 | 24.0 | 6725.0 | 50.0 | 6425.0 | 50.0 |
| 55 | F8.3 | $H\alpha$ (48) | 6562.8 | 48.0 | 6725.0 | 50.0 | 6425.0 | 50.0 |
| 56 | F8.3 | $H\alpha$ (70) | 6562.8 | 70.0 | 6725.0 | 50.0 | 6425.0 | 50.0 |
| 57 | F8.3 | CaH | 6788.0 | 505.0 | 7434.0 | 10.0 | 6532.0 | 5.0 |
| 58 | F8.3 | TiO | 7209.0 | 333.3 | 7434.0 | 10.0 | 6532.0 | 5.0 |
| 59 | F8.3 | CN | 6890.0 | 26.0 | 7795.0 | 10.0 | 6870.0 | 10.0 |
| 60 | F8.3 | O I tri | 7775.0 | 30.0 | 7805.0 | 10.0 | 7728.0 | 10.0 |

Table 2—Continued

| Column | Format | Description | Central (Å) | Width (Å) | Red (Å) | Width (Å) | Blue (Å) | Width (Å) |
|---|---|---|---|---|---|---|---|---|
| 61 | F8.3 | K I | 7687.0 | 34.0 | 8080.0 | 10.0 | 7510.0 | 10.0 |
| 62 | F8.3 | K I | 7688.0 | 95.0 | 8132.0 | 5.0 | 7492.0 | 5.0 |
| 63 | F8.3 | Na I | 8187.5 | 15.0 | 8190.0 | 55.0 | 8150.0 | 10.0 |
| 64 | F8.3 | Na I-red | 8190.2 | 33.0 | 8248.6 | 5.0 | 8140.0 | 5.0 |
| 65 | F8.3 | Ca II (26) | 8498.0 | 26.0 | 8520.0 | 10.0 | 8467.5 | 25.0 |
| 66 | F8.3 | Paschen (13) | 8467.5 | 13.0 | 8570.0 | 14.0 | 8457.0 | 10.0 |
| 67 | F8.3 | Ca II | 8498.5 | 29.0 | 8570.0 | 14.0 | 8479.0 | 10.0 |
| 68 | F8.3 | Ca II (40) | 8542.0 | 40.0 | 8570.0 | 14.0 | 8479.0 | 10.0 |
| 69 | F8.3 | Ca II | 8542.0 | 16.0 | 8600.0 | 60.0 | 8520.0 | 20.0 |
| 70 | F8.3 | Paschen (42) | 8598.0 | 42.0 | 8630.5 | 23.0 | 8570.0 | 14.0 |
| 71 | F8.3 | Ca II | 8662.1 | 16.0 | 8694.0 | 12.0 | 8600.0 | 60.0 |
| 72 | F8.3 | Ca II (40) | 8662.0 | 40.0 | 8712.5 | 25.0 | 8630.5 | 23.0 |
| 73 | F8.3 | Paschen (42) | 8751.0 | 42.0 | 8784.0 | 16.0 | 8712.5 | 25.0 |
| 74 | F7.3 | TiO1 | 6720.5 | 5.0 | 6720.5 | 5.0 | 6705.5 | 5.0 |
| 75 | F7.3 | TiO2 | 7059.5 | 5.0 | 7059.5 | 5.0 | 7044.5 | 5.0 |
| 76 | F7.3 | TiO3 | 7094.5 | 5.0 | 7094.5 | 5.0 | 7081.5 | 5.0 |
| 77 | F7.3 | TiO4 | 7132.5 | 5.0 | 7132.5 | 5.0 | 7117.5 | 5.0 |
| 78 | F7.3 | TiO5 | 7130.5 | 9.0 | 7130.5 | 9.0 | 7044.0 | 4.0 |
| 79 | F7.3 | CaH1 | 6385.0 | 10.0 | 6415.0 | 10.0 | 6350.0 | 10.0 |
| 80 | F7.3 | CaH2 | 6830.0 | 32.0 | 6830.0 | 32.0 | 7044.0 | 4.0 |
| 81 | F7.3 | CaH3 | 6975.0 | 30.0 | 6975.0 | 30.0 | 7044.0 | 4.0 |
| 82 | F7.3 | CaOH | 6235.0 | 10.0 | 6235.0 | 10.0 | 6349.5 | 9.0 |
| 83 | F7.3 | H$\alpha$ | 6563.0 | 6.0 | 6563.0 | 6.0 | 6550.0 | 10.0 |
| 84 | F6.1 | $< S/N >$ | | | | | | |
| 85 | A10 | RV Flag | | | | | | |

Note. — $< S/N >$ is the average signal to noise ratio per pixel over 3850 Å to 6000 Å.

Table 3. Comparison of Parameters from NGS1 and NGS2 grids with the ELODIE and
MILES Libraries and High-Resolution Values

| | | | | $T_{\mathrm{eff}}$ | | $\log g$ | | [Fe/H] | |
|---|---|---|---|---|---|---|---|---|---|
| Grid | Library | $S/N$ | N | $<\Delta>$ | $\sigma$ | $<\Delta>$ | $\sigma$ | $<\Delta>$ | $\sigma$ |
| | | | | (K) | (K) | (dex) | (dex) | (dex) | (dex) |
| NGS1 | | | | | | | | | |
| | ELODIE | Full | 562 | 86 | 96 | +0.10 | 0.24 | −0.17 | 0.14 |
| | ELODIE | 50/1 | 543 | 110 | 104 | −0.01 | 0.28 | −0.20 | 0.13 |
| | ELODIE | 25/1 | 538 | 114 | 118 | −0.05 | 0.32 | −0.18 | 0.16 |
| | ELODIE | 12.5/1 | 489 | 146 | 155 | −0.11 | 0.43 | +0.20 | 0.20 |
| | ELODIE | 6.25/1 | 370 | 149 | 225 | −0.16 | 0.67 | +0.47 | 0.19 |
| | MILES | Full | 367 | 105 | 109 | +0.11 | 0.34 | −0.19 | 0.18 |
| | HIGHRES | Full | 114 | +5 | 137 | +0.00 | 0.30 | −0.12 | 0.17 |
| NGS2 | | | | | | | | | |
| | ELODIE | Full | 557 | ... | ... | +0.12 | 0.26 | −0.23 | 0.16 |
| | MILES | Full | 341 | ... | ... | +0.14 | 0.30 | −0.25 | 0.15 |
| | HIGHRES | Full | 112 | ... | ... | +0.09 | 0.27 | −0.14 | 0.17 |

Note. — HIGHRES is the average of the two high-resolution
analyses.

Table 4.   Brief Descriptions of SSPP Flags

| Flag | Comment |
| --- | --- |
| n | All appears normal |
| D | Likely white dwarf |
| d | Likely sdO or sdB |
| H | Hot star with $T_{\text{eff}} > 10000$ K |
| h | Helium line detected, possibly very hot star |
| l | Likely solar abundance, late-type star |
| E | Emission lines in spectrum |
| S | Sky spectrum |
| V | No radial velocity information available |
| N | Noisy spectrum at extrema |
| C | The photometric $g - r$ color may be incorrect |
| B | Unexpected H$\alpha$ line strength predicted from H$\delta$ |
| G | Strong G-band feature |
| g | Mild G-band feature |

Table 5.   Valid Ranges of Effective Temperature, $g - r$ Color, and $S/N$ for Individual
Methods in the SSPP

**Temperature**

| Method | T1 | T2 | T3 | T4 | T5 | T6 | T7 | T8 | T9 | T10 |
|---|---|---|---|---|---|---|---|---|---|---|
| | $HA24$ | $HD24$ | K-MOD | G-ISO | EMP | NGS1 | ANN | WBG99 | k24 | ki13 |
| $T_{\rm eff}$[1] | $4.5 - 8.5$ | $5.5 - 8.5$ | $4 - 10$ | $4 - 10$ | $4 - 8$ | $4 - 8$ | $5 - 7.5$ | $4.5 - 10$ | $5 - 7$ | $5 - 7$ |
| $g - r$ | $0.0 - 0.8$ | $0.0 - 0.6$ | $-0.2 - 1.2$ | $0.0 - 1.2$ | $-0.2 - 1.2$ | $0.0 - 1.2$ | $0.1 - 0.7$ | $-0.2 - 0.8$ | $0.1 - 0.7$ | $0.1 - 0.7$ |
| $S/N$ | ... | ... | ... | ... | ... | $> 10.0$ | $> 10.0$ | $> 10.0$ | $> 10.0$ | $> 10.0$ |
| $S/N$ ($g - r < 0.3$) | ... | ... | ... | ... | ... | $> 20.0$[2] | $> 15.0$ | $> 15.0$ | $> 15.0$ | $> 15.0$ |

**Gravity**

| Method | G1 | G2 | G3 | G4 | G5 | G6 | G7 | G8 |
|---|---|---|---|---|---|---|---|---|
| | NGS2 | NGS1 | ANN | CaI | MgH | WBG | k24 | ki13 |
| $T_{\rm eff}$[1] | $5 - 8$ | $5 - 8$ | $5 - 7.5$ | $4.5 - 6$ | $4.5 - 6$ | $4.5 - 10$ | $5 - 7$ | $5 - 7$ |
| $g - r$ | $0.0 - 0.7$ | $0.0 - 0.7$ | $0.1 - 0.7$ | $0.4 - 0.9$ | $0.4 - 0.9$ | $-0.2 - 0.8$ | $0.1 - 0.7$ | $0.1 - 0.7$ |
| $S/N$ | $> 10.0$ | $> 10.0$ | $> 10.0$ | $> 10.0$ | $> 10.0$ | $> 10.0$ | $>10.0$ | $> 10.0$ |
| $S/N$ ($g - r < 0.3$) | $> 20.0$[2] | $> 20.0$[2] | $> 15.0$ | ... | ... | $> 15.0$ | $> 15.0$ | $> 15.0$ |

**Metallicity**

| Method | M1 | M2 | M3 | M4 | M5 | M6 | M7 | M8 | M9 |
|---|---|---|---|---|---|---|---|---|---|
| | NGS2 | NGS1 | ANN | CaII K | ACF | CaII T | WBG | k24 | ki13 |
| $T_{\rm eff}$[1] | $4 - 8$ | $4 - 8$ | $5 - 7.5$ | $5 - 7$ | ... | ... | $4.5 - 10$ | $5 - 7$ | $5 - 7$ |
| $g - r$ | $0.0 - 1.2$ | $0.0 - 1.2$ | $0.1 - 0.7$ | $0.1 - 0.7$ | ... | ... | $-0.2 - 0.8$ | $0.1 - 0.7$ | $0.1 - 0.7$ |
| $S/N$ | $> 10.0$ | $> 10.0$ | $> 10.0$ | $> 10.0$ | ... | ... | $> 10.0$ | $> 10.0$ | $> 10.0$ |
| $S/N$ ($g - r < 0.3$) | $> 20.0$[2] | $> 20.0$[2] | $> 15.0$ | $> 15.0$ | ... | ... | $> 15.0$ | $> 15.0$ | $> 15.0$ |

[1]$T_{\rm eff}$ is in units of 1000 K.

[2]In hhis case, $g - r < 0.4$

Note. — $S/N$ is the average signal to noise ratio per pixel over 3850 Å to 6000 Å. $HA24$ and $HD24$ are the temperature estimates from the Hα and Hδ line index in 24 Å widths, respectively. The temperature estimated from Kurucz models is referred to as K-MOD; G-ISO is for the Girardi et al. (2004) isochrones. EMP is the temperature determined by equation 12. These temperature estimates are used only if the color flag is not raised and the mean of these five temperature estimates are greater than 7500 K or less than 4500 K. ANN is the neural network approach. ACF is the Autocorrelation Function method, and Ca II T is based on the Ca II triplet line index. [Fe/H] estimates from these approaches are not used at by the SSPP at present. WBG99 is the method from Wilhelm, Beers, & Gray (1999).

Table 6.  Comparison of $T_{\rm eff}$ Estimates from Individual Methods with Those from Two
High-Resolution Analyses

|  |  | AD | T1 | T2 | T3 | T4 | T5 | T6 | T7 | T8 | T9 | T10 |
|---|---|---|---|---|---|---|---|---|---|---|---|---|
| HA1 | N | 81 | 81 | 81 | 81 | 81 | 81 | 81 | 74 | 81 | 76 | 76 |
|  | $<\Delta>$ | +183 | +93 | +194 | +124 | +41 | +142 | +145 | +162 | +228 | +329 | +127 |
|  | $\sigma$ | 169 | 138 | 186 | 285 | 244 | 259 | 171 | 186 | 194 | 223 | 202 |
| HA2 | N | 124 | 123 | 125 | 125 | 125 | 125 | 124 | 111 | 122 | 115 | 115 |
|  | $<\Delta>$ | −30 | −137 | −27 | −108 | −180 | −82 | −74 | −73 | −8 | +48 | −100 |
|  | $\sigma$ | 145 | 191 | 312 | 163 | 207 | 186 | 177 | 149 | 200 | 177 | 182 |
| MEAN | N | 124 | 123 | 125 | 125 | 125 | 125 | 124 | 111 | 122 | 115 | 115 |
|  | $<\Delta>$ | +55 | −18 | +74 | −41 | −85 | −4 | +10 | +28 | +85 | +148 | −6 |
|  | $\sigma$ | 123 | 158 | 228 | 198 | 206 | 188 | 133 | 144 | 182 | 203 | 167 |

Note. — 'AD' is the adopted estimate of $T_{\rm eff}$. 'HA1' indicates the analysis performed by C.A.; 'HA2' indicates the analysis performed by T.S.. 'MEAN' is the average of the two analyses. 'N' is the number of stars compared. $<\Delta>$ is the mean from a Gaussian fit to the residuals of $T_{\rm eff}$ between the SSPP and the high-resolution analysis; $\sigma$ is the standard deviation of the fit.

Table 7.   Comparison of log $g$ Estimates from Individual Methods with Those from Two
High-Resolution Analyses

|  |  | AD | G1 | G2 | G3 | G4 | G5 | G6 | G7 | G8 |
|---|---|---|---|---|---|---|---|---|---|---|
| HA1 | N | 81 | 74 | 76 | 74 | 34 | 34 | 81 | 76 | 76 |
|  | $< \Delta >$ | +0.09 | +0.15 | +0.07 | −0.16 | +0.21 | −0.02 | −0.31 | +0.37 | +0.25 |
|  | $\sigma$ | 0.23 | 0.19 | 0.18 | 0.29 | 0.40 | 0.13 | 0.93 | 0.33 | 0.30 |
| HA2 | N | 124 | 114 | 116 | 111 | 54 | 54 | 122 | 115 | 115 |
|  | $< \Delta >$ | +0.03 | +0.04 | −0.01 | −0.18 | +0.13 | +0.02 | −0.26 | +0.31 | +0.13 |
|  | $\sigma$ | 0.32 | 0.37 | 0.38 | 0.55 | 0.42 | 0.28 | 0.87 | 0.37 | 0.44 |
| MEAN | N | 124 | 114 | 116 | 111 | 54 | 54 | 122 | 115 | 115 |
|  | $< \Delta >$ | +0.04 | +0.08 | +0.01 | −0.16 | +0.15 | +0.04 | −0.29 | +0.35 | +0.18 |
|  | $\sigma$ | 0.25 | 0.26 | 0.29 | 0.42 | 0.40 | 0.27 | 0.89 | 0.33 | 0.41 |

Table 8.   Comparison of [Fe/H] Estimates from Individual Methods with Those from Two
High-Resolution Analyses

|  |  | AD | BI | RE | M1 | M2 | M3 | M4 | M5 | M6 | M7 | M8 | M9 |
|---|---|---|---|---|---|---|---|---|---|---|---|---|---|
| HA1 | N | 81 | 81 | 81 | 80 | 80 | 74 | 74 | 79 | 79 | 81 | 76 | 76 |
|  | $< \Delta >$ | $-0.08$ | $-0.06$ | $-0.14$ | $-0.23$ | $-0.19$ | $-0.16$ | $+0.07$ | $-0.47$ | $+0.50$ | $+0.10$ | $+0.05$ | $+0.12$ |
|  | $\sigma$ | 0.16 | 0.16 | 0.17 | 0.13 | 0.15 | 0.18 | 0.35 | 0.31 | 0.35 | 0.24 | 0.17 | 0.15 |
| HA2 | N | 124 | 124 | 124 | 123 | 123 | 111 | 110 | 122 | 118 | 122 | 115 | 115 |
|  | $< \Delta >$ | $-0.00$ | $+0.01$ | $-0.04$ | $-0.07$ | $-0.06$ | $-0.10$ | $+0.07$ | $-0.30$ | $+0.63$ | $+0.15$ | $+0.13$ | $+0.15$ |
|  | $\sigma$ | 0.28 | 0.27 | 0.31 | 0.23 | 0.25 | 0.30 | 0.47 | 0.39 | 0.51 | 0.43 | 0.33 | 0.30 |
| MEAN | N | 124 | 124 | 124 | 123 | 123 | 111 | 110 | 122 | 118 | 122 | 115 | 115 |
|  | $< \Delta >$ | $-0.04$ | $-0.03$ | $-0.08$ | $-0.13$ | $-0.11$ | $-0.12$ | $+0.04$ | $-0.35$ | $+0.58$ | $+0.12$ | $+0.10$ | $+0.14$ |
|  | $\sigma$ | 0.21 | 0.21 | 0.22 | 0.17 | 0.18 | 0.23 | 0.42 | 0.39 | 0.49 | 0.34 | 0.24 | 0.20 |